

Rock mass strength and elastic modulus of the Buntsandstein: An important lithostratigraphic unit for geothermal exploitation in the Upper Rhine Graben



Michael J. Heap^{a,*}, Marlène Villeneuve^b, Alexandra R.L. Kushnir^a, Jamie I. Farquharson^{a,c}, Patrick Baud^a, Thierry Reuschlé^a

^a Géophysique Expérimentale, Institut de Physique de Globe de Strasbourg (UMR 7516 CNRS, Université de Strasbourg/EOST), 5 rue René Descartes, 67084 Strasbourg cedex, France

^b Department of Geological Sciences, University of Canterbury, Private Bag 4800, Christchurch, New Zealand

^c Department of Marine Geosciences, Rosenstiel School of Marine and Atmospheric Sciences, University of Miami, 4600 Rickenbacker Causeway, Miami, United States

ARTICLE INFO

Keywords:

Buntsandstein
Uniaxial compressive strength
Triaxial deformation experiments
Porosity
Clay content
Geothermal reservoir

ABSTRACT

Geothermal exploitation in the Upper Rhine Graben increasingly targets the interface between the granitic basement and the overlying Buntsandstein unit. Results from deformation experiments are combined with structural assessments to provide reservoir-scale wet and dry strength and elastic modulus profiles for the Buntsandstein at Soultz-sous-Forêts (France). Our analysis finds five zones characterised by low strength and elastic modulus. The strength and elastic modulus of “massive” zones are lower when the rock is wet (i.e. water-saturated), highlighting the importance of performing wet deformation experiments for geothermal rock mass assessments. These data and methods can be used to provide assessments of other geothermal sites within the region to assist prospection, stimulation, and optimisation strategies.

1. Introduction

An understanding of the strength and elastic modulus of rock within a geothermal reservoir is an important input in models that guide reservoir prospection, stimulation, and optimisation strategies. Laboratory experiments designed to measure these parameters are typically performed on samples with dimensions shorter than the meso- or macrofracture length scale. As a result, laboratory data gathered on nominally intact rock cannot be directly applied to large-scale geotechnical practices. Although upscaling laboratory values to the reservoir- or borehole-scale is non-trivial, widely used empirical geotechnical tools exist to bridge this length scale discrepancy. Two equations from the geotechnical toolbox, which provide estimates for rock mass strength and rock mass elastic modulus, respectively, are the generalised Hoek-Brown failure criterion (Hoek et al., 2002) and the Hoek-Diederichs equation (Hoek and Diederichs, 2006). Both of these approaches take an assessment of the rock mass structure (e.g., fracture density) and the surface condition of the fractures (e.g., smooth/rough, the pervasiveness of weathering or alteration, the nature of the fracture infilling) into account to determine the rock mass strength and elastic modulus, which will be often less than that of the intact material.

Geothermal energy exploitation is common in the Upper Rhine Graben, a 350 km-long and 50 km-wide Cenozoic rift valley that extends from Frankfurt (Germany) down to Basel (Switzerland), due to the presence of anomalously high thermal gradients (areas of geothermal interest typically have thermal gradients > 80 °C) attributed to hydrothermal circulation within the fractured Palaeozoic granitic basement and the overlying Permian and Triassic sedimentary rocks (e.g., Pribnow and Schellschmidt, 2000; Buchmann and Connolly, 2007; Guillou-Frottier et al., 2013; Baillieux et al., 2013; Magnenet et al., 2014; Freymark et al., 2017). A total of 15 geothermal wells have been drilled (to depths between ~1000 and ~5000 m) in the Upper Rhine Graben since the 1980s (Vidal and Genter, 2018) and notable geothermal sites include Soultz-sous-Forêts (e.g., Kapelmeyer et al., 1991; Baria et al., 1999; Gérard et al., 2006; Fig. 1) and Rittershoffen (e.g., Baujard et al., 2017; Glaas et al., 2018; Fig. 1) in France, Brühl (e.g., Bauer et al., 2017), Insheim, Trebur, and Bruchsal in Germany, and Riehen in Switzerland.

A recent study (Villeneuve et al., 2018) provided rock mass strengths (using the generalised Hoek-Brown failure criterion; Hoek et al., 2002) and elastic moduli (using the Hoek-Diederichs equation; Hoek and Diederichs, 2006) for the fractured Palaeozoic granitic

* Corresponding author.

E-mail address: heap@unistra.fr (M.J. Heap).

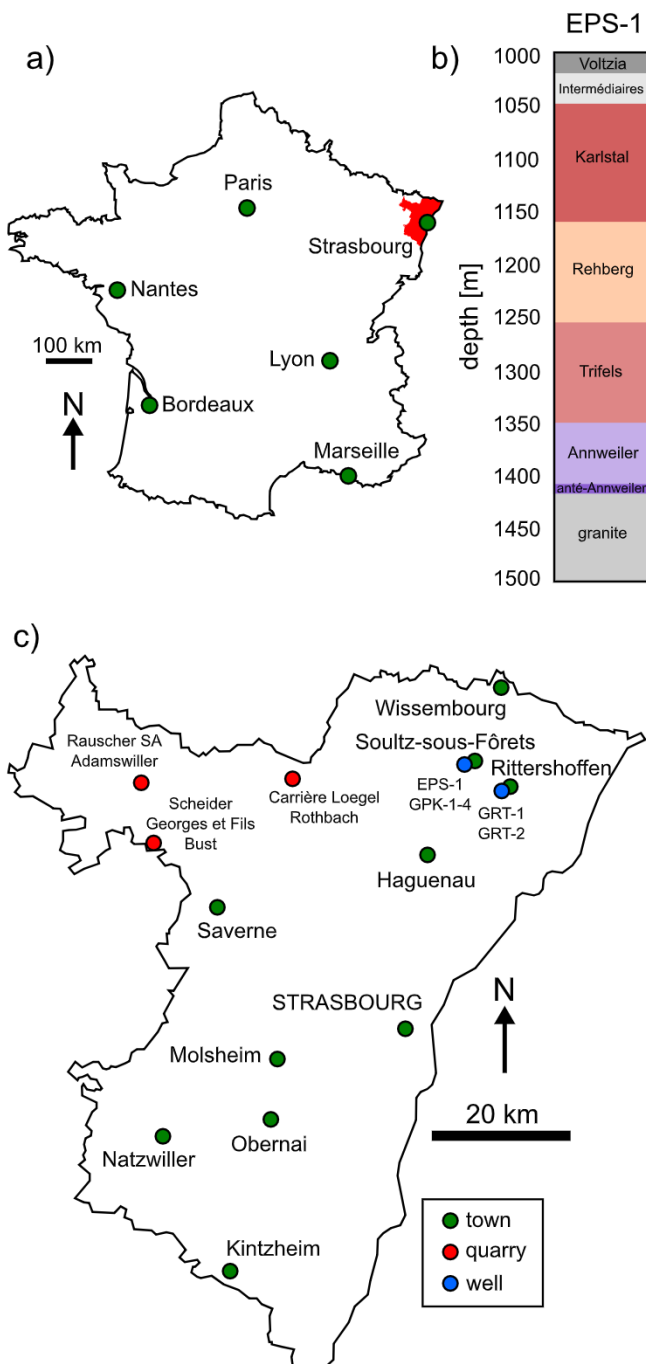


Fig. 1. (a) Map of France showing the location of the Bas-Rhin (Lower Rhine) department of Alsace (in red). (b) Stratigraphic column showing the units within the Buntsandstein from exploration well EPS-1 at Soultz-sous-Forêts (Alsace, France). The granite basement is encountered at a depth of 1417 m. Depths are measured depths. (c) Map of the Bas-Rhin (Lower Rhine) department of Alsace (shown in red in panel (a)) showing the location of the major cities/towns (green circles), the geothermal sites of Soultz-sous-Forêts and Rittershoffen (green circles), the wells EPS-1, GPK-1-4, and GRT-1-2 (blue circles), and the locations and names of the quarries (red circles). (For interpretation of the references to colour in this figure legend, the reader is referred to the web version of this article).

basement from exploration well EPS-1 at the Soultz-sous-Forêts geothermal site (Fig. 1) using laboratory experiments on intact material and structural data from core analyses. Our goal here, using the same approach, is to provide estimates of borehole-scale rock mass strength and elastic modulus for the lowermost overlying Permian and Triassic

sedimentary rocks sampled from exploration well EPS-1 (located about 1 km southwest of Soultz-sous-Forêts; Fig. 1), from a depth of 1008 to 1414 m (i.e. the Buntsandstein lithostratigraphic unit). The reasons for choosing Soultz-sous-Forêts as a case study are twofold. First, the Buntsandstein was continuously cored at exploration well EPS-1 (to a core diameter of 78 mm), providing the samples required for laboratory testing (uniaxial and triaxial compression experiments). Second, there exists a wealth of structural data (fracture density and fracture fill, for example) for the borehole at EPS-1, providing the data required for the assessment of rock mass structure. Since the Buntsandstein is known to be laterally extensive (Aichholzer et al., 2016; Vidal and Genter, 2018), the results of this study can not only be used to help optimise current geothermal sites in the Upper Rhine Graben, but also to help guide and optimise future geothermal sites currently in development, such as those at Illkirch and Vendenheim (both in Alsace, France). One of the principal motivations for this study is that recent (e.g., Rittershoffen; Baujard et al., 2017; Fig. 1) and future geothermal exploitation in the Upper Rhine Graben has and will target the interface between the granitic basement and the overlying Permian and Triassic sedimentary rocks.

Providing estimates of rock mass strength and elastic modulus for the Buntsandstein is complicated for two principal reasons. First, the petrophysical variability of the Buntsandstein (e.g., Vernoux et al., 1995; Aichholzer et al., 2016; Heap et al., 2017) demands that the intact rock properties (strength and elastic modulus) are characterised for materials sampled from a number of different depths. Although the assumption of mechanical homogeneity (i.e. similar intact strength and elastic modulus at different depths) was justified when providing rock mass properties of the porphyritic granite (monzogranite) from EPS-1 from a depth of 1414 to 2200 m (Villeneuve et al., 2018), the mechanical properties of the Buntsandstein vary considerably due to the variability in porosity and microstructural attributes such as pore size and grain size (Vernoux et al., 1995; Haffen et al., 2013; Griffiths et al., 2016; Heap et al., 2017; Kushnir et al., 2018a), parameters known to greatly influence the strength and stiffness of rocks, including sandstone (e.g., Palchik, 1999; Chang et al., 2006; Baud et al., 2014). Here, therefore, we perform systematic laboratory measurements on material sampled at regular depth intervals (from 1008 to 1414 m) from the EPS-1 core at the Soultz-sous-Forêts geothermal site. Second, experimental studies have shown that clay plays an important role in the observed weakening of sandstone in the presence of water (e.g., Rutter and Mainprice, 1978; Hawkins and McConnell, 1992; Baud et al., 2000; Demarco et al., 2007). For example, Hawkins and McConnell (1992) found that the uniaxial compressive strength (UCS) of sandstone was reduced by 78% for clay-rich sandstones and by only 8% for siliceous sandstones in the presence of water. The variable, and sometimes high, clay contents of the Buntsandstein sandstones (e.g., Heap et al., 2017) thus calls into question the use of laboratory strength and elastic moduli data determined for dry rocks typically used in geotechnical rock mass assessments. Therefore, here we perform dry and wet laboratory deformation measurements to provide estimations of the dry and wet rock mass strength and elastic modulus for the Buntsandstein unit at the Soultz-sous-Forêts geothermal site.

2. Methods and materials

2.1. Intact failure criteria

The strength of intact rock, including sandstone, in the brittle regime increases with increasing confining pressure or depth (e.g., Wong et al., 1997; Baud et al., 2000; Bésuelle et al., 2003). The Hoek-Brown failure criterion for intact rock is an empirical failure criterion that provides strength estimates for intact rock at depth using the uniaxial compressive strength, C_o , (i.e. the strength of the rock at ambient pressure) and a constant, m_i :

$$\sigma'_1 = \sigma'_3 + C_o \left(m_i \frac{\sigma'_3}{C_o} + 1 \right)^{0.5} \quad (1)$$

where σ'_1 and σ'_3 are the effective maximum and minimum principal stresses, respectively. The unitless constant m_i describes the shape of the failure envelope on a graph of σ'_1 as a function of σ'_3 , and is therefore related to the microstructural and mineralogical attributes of the rock (mineral content, grain size, grain shape, pore size, and pore shape, amongst many others) (Eberhardt, 2012). The most reliable method to determine m_i is to run a series of triaxial deformation experiments on the rock of interest (Hoek and Brown, 1980); however values of m_i are often estimated using charts that offer values for common lithologies (e.g., Hoek and Brown, 1997).

In this study, C_o is determined for samples of Buntsandstein sandstone taken from regular depth intervals (every 40–50 m) from the continuous core available at the EPS-1 exploration well (Fig. 1). Values of empirical constant m_i are often taken from tables of “standard” values for common lithologies; the recommended value of m_i for sandstone is 19 (Hoek and Brown, 1997). However, in our study, we chose instead to perform a suite of triaxial experiments on samples from one of the sampled depth intervals in order to better constrain m_i for the Buntsandstein (see Section 2.6). Uniaxial experiments were performed under both dry and wet conditions to provide the dry intact uniaxial strength, C_{o_d} , and the wet intact uniaxial strength, C_{o_w} (see Section 2.5). Similarly, wet and dry triaxial experiments provide estimates for m_i under dry conditions, m_{i_d} , and under wet conditions, m_{i_w} (see Section 2.6). Therefore, Eq. (1) can be modified to provide the intact rock strength with depth for dry (Eq. (2)) and wet rock (Eq. (3)), respectively:

$$\sigma'_1 = \sigma'_3 + C_{o_d} \left(m_{i_d} \frac{\sigma'_3}{C_o} + 1 \right)^{0.5} \quad (2)$$

$$\sigma'_1 = \sigma'_3 + C_{o_w} \left(m_{i_w} \frac{\sigma'_3}{C_o} + 1 \right)^{0.5} \quad (3)$$

2.2. Rock mass strength failure criteria

Rock mass strength can be determined using the generalised Hoek-Brown failure criterion:

$$\sigma'_1 = \sigma'_3 + C_o \left(m_b \frac{\sigma'_3}{C_o} + s \right)^a \quad (4)$$

where m_b , s , and a are unitless fitting parameters for a fractured rock mass and are defined as follows (Hoek et al., 2002):

$$m_b = m_i e^{\left(\frac{GSI-100}{28-14D}\right)} \quad (5)$$

$$s = e^{\left(\frac{GSI-100}{9-3D}\right)} \quad (6)$$

$$a = \frac{1}{2} + \frac{1}{6} \left(e^{-\frac{GSI}{15}} + e^{-\frac{20}{3}} \right) \quad (7)$$

where D is a unitless disturbance factor related to blasting damage in large excavations (since well drilling does not use explosives, $D = 0$ in our case study; we provide the full equation here for completeness) and GSI is the Geological Strength Index, a unitless value that describes the rock mass characteristics (Marinos et al., 2005). Values of GSI range from 0 to 100, where high values indicate intact or massive rock masses with fresh surfaces and low values indicate blocky/disintegrated/laminated rock masses with highly weathered surfaces and clay coatings or fillings (Marinos et al., 2005). GSI is typically obtained from rock outcrop exposures, but for this study values of GSI were determined using structural data collected on the EPS-1 core material (see Section 2.7), as described in Villeneuve et al. (2018). Eq. (4) can be recast to provide the rock mass strength with depth for dry (Eq. (8)) and wet rock

(Eq. (9)), respectively:

$$\sigma'_1 = \sigma'_3 + C_{o_d} \left(m_{b_d} \frac{\sigma'_3}{C_{o_d}} + s \right)^a \quad (8)$$

$$\sigma'_1 = \sigma'_3 + C_{o_w} \left(m_{b_w} \frac{\sigma'_3}{C_{o_w}} + s \right)^a \quad (9)$$

where m_{b_d} and m_{b_w} are given as, respectively:

$$m_{b_d} = m_{i_d} e^{\left(\frac{GSI-100}{28-14D}\right)} \quad (10)$$

$$m_{b_w} = m_{i_w} e^{\left(\frac{GSI-100}{28-14D}\right)} \quad (11)$$

2.3. Intact and rock mass elastic modulus

The elastic modulus of intact rock, E_i , can be determined from the elastic portion of the stress-strain curve of a rock deforming in compression. The rock mass elastic modulus, E_{rm} , can be determined using the Hoek-Diederichs equation (Hoek and Diederichs, 2006):

$$E_{rm} = E_i \left(0.02 + \frac{1 - \frac{D}{2}}{1 + e^{((60+15D-GSI)/11)}} \right) \quad (12)$$

As for the rock strength equations in Section 2.2, the disturbance factor D is equal to zero for our application. As mentioned in Section 2.2, values of GSI were determined using structural data collected on the EPS-1 core material (see Section 2.7). Eq. (12) can be modified to provide values for the elastic modulus of a dry (Eq. (13)) and wet rock mass (Eq. (14)), respectively:

$$E_{rm_d} = E_{i_d} \left(0.02 + \frac{1 - \frac{D}{2}}{1 + e^{((60+15D-GSI)/11)}} \right) \quad (13)$$

$$E_{rm_w} = E_{i_w} \left(0.02 + \frac{1 - \frac{D}{2}}{1 + e^{((60+15D-GSI)/11)}} \right) \quad (14)$$

where E_{i_d} and E_{i_w} are the intact elastic moduli of dry and wet rock, respectively.

2.4. Experimental materials and sample preparation

The Buntsandstein lithostratigraphic unit was sampled at regular (~40–50 m) depth intervals (between 1008 to 1414 m; Fig. 1b) from the EPS-1 exploration well at the Soultz-sous-Forêts geothermal site (Figs. 1 and 2). This Permian and Triassic sedimentary unit (described in, for example, Vernoux et al., 1995; Haffen et al., 2013; Vidal et al., 2015; Aichholzer et al., 2016; Griffiths et al., 2016; Heap et al., 2017; Kushnir et al., 2018a) directly overlies the fractured Palaeozoic granitic reservoir (described in, for example, Genter and Trainea, 1996; Genter et al., 1997; Sausse et al., 2006; Dezayes et al., 2010; Genter et al., 2010). We collected 1 m-long pieces of the 78 mm-diameter core at each of the sampled depths. In total, twelve depths were sampled (one sandstone from the Voltzia unit, one from the Couches Intermédiaires unit, three from the Karlstal unit, two from the Rehberg unit, two from the Trifels unit, two from the Annweiler unit, and one from the Anté-Annweiler unit; Fig. 1b). Four or five cylindrical samples, 20, 18.75, or 12 mm in diameter (depending on the strength of the sandstone), were cored from each of the twelve cores collected and precision-ground to a nominal length of 40, 37.5, or 24 mm, respectively. These samples were cored so that their axes were parallel to the EPS-1 borehole (i.e. perpendicular to bedding; Fig. 2). We complement these borehole samples with samples prepared from blocks (all from the Buntsandstein) acquired from local quarries (from Rothbach, Adamswiller, and Bust, all in France; see Fig. 1c for quarry locations). Samples from the quarry

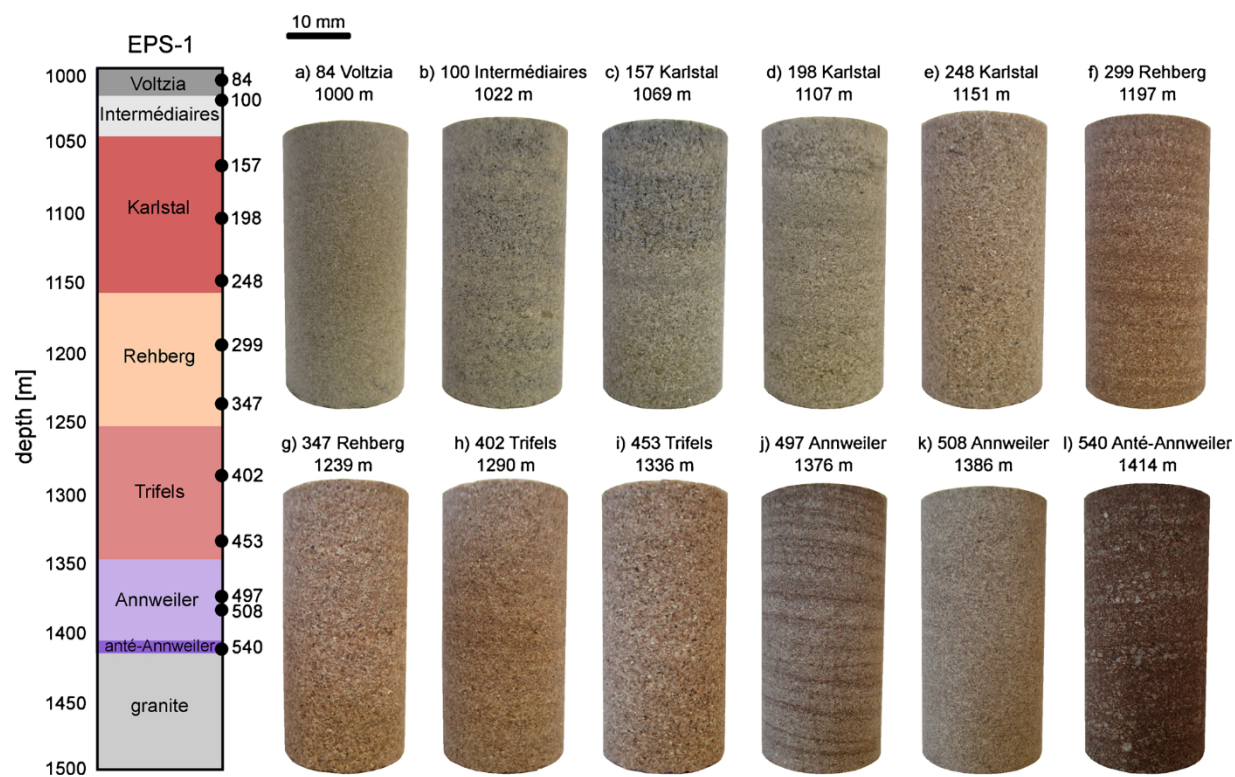


Fig. 2. Photographs of each of the twelve sandstones (20 mm diameter core samples nominally 40 mm in length) sampled from exploration well EPS-1 at Soultz-sous-Forêts. The box number, lithological unit, and depth are given above each sample. A stratigraphic column showing the units within the Buntsandstein from exploration well EPS-1 at Soultz-sous-Forêts (Alsace, France) is shown on the left hand side. The locations for each of the sampled depths are indicated on the stratigraphic column.

blocks were cored perpendicular to bedding to a diameter of 20 mm and precision-ground to a nominal length of 40 mm. All of the samples were washed using tapwater and then dried in a vacuum oven at 40 °C for at least 48 h.

The twelve samples collected from exploration well EPS-1 are feldspathic (> 10 wt.% feldspar) or quartz-rich (< 10 wt.% feldspar) sandstones that contain variable amounts of pore-filling clay (muscovite/illite-smectite) (from 2 to 13.1 wt.%) (Fig. 3; Table 1; Heap et al., 2017). Most of the sandstones are homogeneous at the sample scale, although a few (in particular samples 299, 497, and 540) contain obvious bedding-parallel laminations (Fig. 2). The average grain diameter of these samples varies from 142 to 424 µm (Fig. 3; Table 2; Heap et al., 2017). The microstructural and textural features of these samples are summarised in Table 2, and are described at length in Heap et al. (2017). The three quarry rocks are all feldspathic sandstones (Table 1). The sandstones from Bust and Adamswiller do not contain any obvious laminations bedding, although the Adamswiller sandstone is known to exhibit a mechanical anisotropy (Baud et al., 2005). Rothbach sandstone, a rock that also shows significant mechanical anisotropy (Louis et al., 2009), however, contains alternating layers that show differences in grain size and porosity (Louis et al., 2005).

Before the samples were deformed, their connected porosity was determined using the connected (skeletal) volume measured by a helium pycnometer (Micromeritics AccuPyc II 1340) and the bulk volume calculated using the sample dimensions.

2.5. Determining C_o (intact uniaxial compressive strength) and E_i (intact elastic modulus)

The prepared cylindrical samples were deformed uniaxially at a strain rate of $1.0 \times 10^{-6} \text{ s}^{-1}$ until macroscopic failure. Half of the samples were deformed “dry” (dried at 40 °C in a vacuum-oven for at least 48 h prior to deformation) and half were deformed “wet”

(vacuum-saturated in deionised water and deformed in a water bath) (see Heap et al., 2014) for a schematic of the experimental device). A lubricating wax was applied to the end-faces of the dry samples to avoid problems associated with the friction between the sample and the pistons. We chose to deform the samples at a relatively low strain rate of $1.0 \times 10^{-6} \text{ s}^{-1}$ to ensure drainage in the low-porosity, low-permeability samples deformed under saturated conditions. During deformation, axial displacement and axial load were measured using a linear variable differential transducer (LVDT) and a load cell, respectively. These measurements were converted to axial strain and axial stress using the sample dimensions. C_{o-d} and C_{o-w} were taken as the peak stress obtained in these uniaxial compressive strength tests under dry and wet conditions, respectively. Values of E_{i-d} and E_{i-w} were determined using the slope of the linear elastic portion of the dry and wet uniaxial stress-strain curves, respectively (Ulusay and Hudson, 2007).

2.6. Determining m_i

The unitless parameter m_i describes the shape of the failure envelope on a graph of σ'_1 as a function of σ'_3 (i.e. the principal stress space). We determined m_i using triaxial experiments conducted on dry and wet cylindrical cores (20 mm in diameter and 40 mm in length) prepared from the core sampled from a depth of 1239 m (from the Rehberg unit; porosity 0.18). Constant strain rate ($1.0 \times 10^{-6} \text{ s}^{-1}$) triaxial experiments were performed at constant effective pressures (defined here as the confining pressure minus the pore fluid pressure) of 2.5, 5, 7.5, 10, and 15 MPa. Samples deformed under dry conditions were therefore deformed at constant confining pressures of 2.5, 5, 7.5, 10, and 15 MPa (pore pressure = 0 MPa). A lubricating wax was applied to the end-faces of the dry samples to avoid problems associated with the friction between the sample and the pistons. Samples deformed under wet conditions were deformed using a constant pore fluid (deionised water) pressure of 10 MPa, and confining pressures of 12.5,

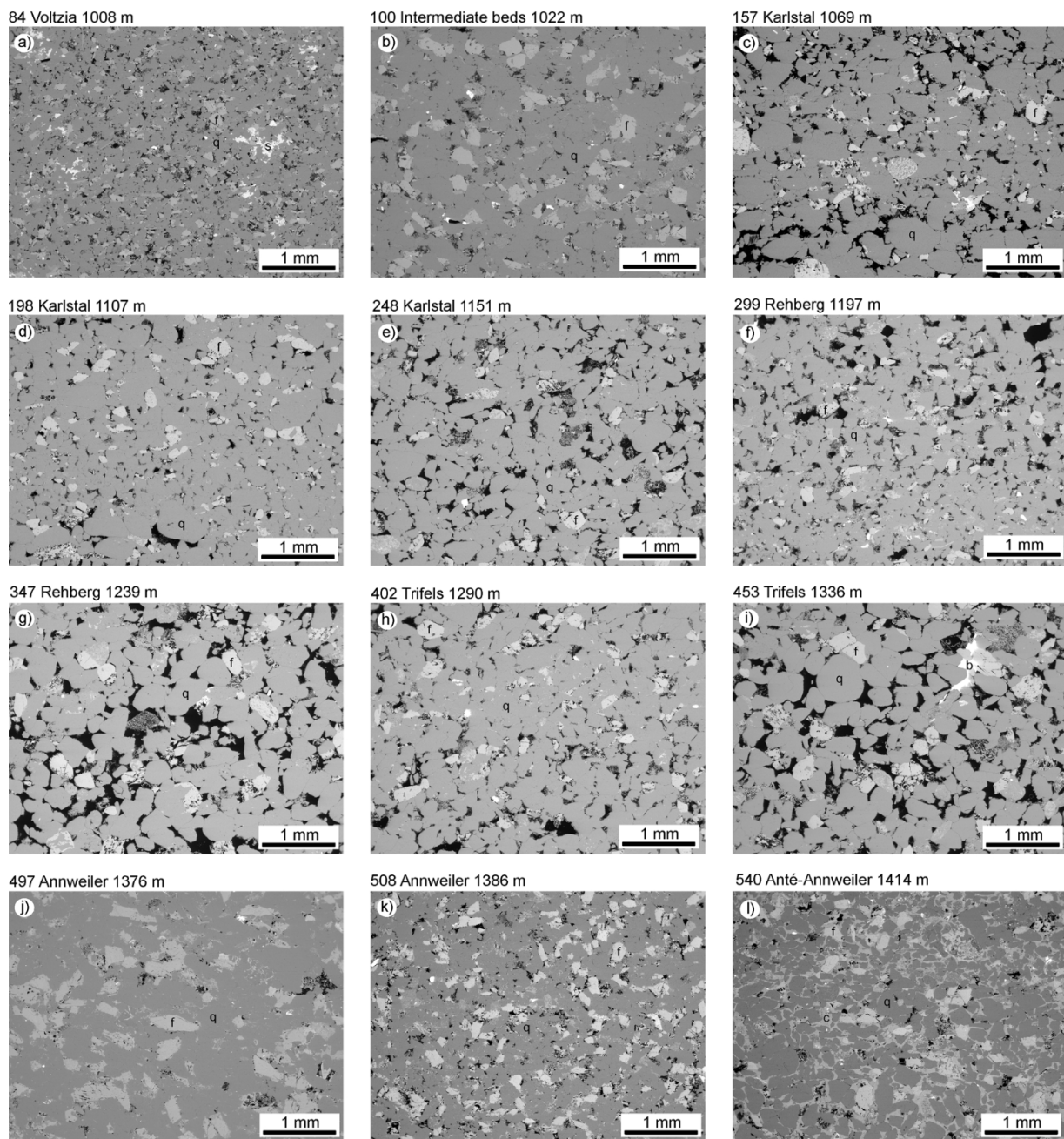


Fig. 3. Backscattered scanning electron microscope (BSE) images for each of the twelve sandstones sampled from exploration well EPS-1 at Soultz-sous-Forêts. The box number, lithological unit, and depth are given above each image. q – quartz; f – feldspar; s – siderite; b – barite; c – clay.

15, 17.5, 20, and 25 MPa. The confining and pore pressures were maintained constant during deformation using a confining and pore fluid pressure intensifier, respectively. During deformation, axial displacement and axial load were measured using an LVDT and a load cell, respectively. These measurements were converted to axial strain and axial stress using the sample dimensions. We determined m_{i-d} and m_{i-w} using the compressive strengths measured for these experiments using the data fitting function (modified cuckoo fit algorithm, basic error summation, and absolute error type) in RocData (Rocscience Inc, 2017).

2.7. Determining the Geological Strength Index (GSI)

The GSI is a unitless value that describes the rock mass characteristics using an assessment of the rock mass structure (e.g., fracture

density) and the surface condition of the fractures (e.g., smooth/rough, the pervasiveness of weathering or alteration, the nature and thickness of the fracture infilling) (Marinos et al., 2005). The logging data from EPS-1 in the Bundsandstein contains the type, location (depth), orientation, infilling type, and infilling thickness of all discontinuities mapped along the core. The locations (depths) were used to derive a fracture frequency. The discontinuity type, infilling type, and infilling thickness were used to assess the joint condition. The rock mass structure and surface condition were assigned broad descriptors, such as “blocky” and “poor”, respectively, which were then used to determine a GSI value using a visual look-up chart (Marinos et al., 2005). Due to the available logging data and core photographs, we consider that our GSI estimates lack the subjectivity often associated with estimates of GSI.

The determination of the surface quality is relatively

Table 1

X-ray powder diffraction (XRPD) analysis showing quantitative bulk mineralogical composition for the twelve sandstones sampled from exploration well EPS-1 at the Soultz-sous-Forêts geothermal site and the three quarry rocks. Values in wt.%. Data from [Heap et al. \(2017\)](#).

Box number	Depth (m)	Unit	Quartz	Orthoclase	Microcline	Muscovite Illite-smectite	Dolomite	Siderite	Hematite	Kaolinite	Chlorite
84	1008	Voltzia	74.5 ± 1.6	3.7 ± 1.9	9.3 ± 0.8	6.0 ± 2.9	4.7 ± 0.1	1.9 ± 0.2	–	–	–
100	1022	Intermédiaires	78.9 ± 1.7	5.6 ± 0.0	9.7 ± 0.5	5.0 ± 2.5	1.0 ± 0.3	–	–	–	–
157	1069	Karlstal	89.2 ± 0.4	4.6 ± 1.1	4.0 ± 1.7	2.0 ± 0.8	0.2 ± 0.1	–	–	–	–
198	1107	Karlstal	89.0 ± 1.1	3.2 ± 0.2	4.6 ± 0.0	3.2 ± 1.3	–	–	–	–	–
248	1151	Karlstal	90.7 ± 1.2	1.9 ± 0.1	4.5 ± 0.2	2.8 ± 1.3	–	–	0.2 ± 0.1	–	–
299	1197	Rehberg	83.4 ± 2.6	1.7 ± 0.2	7.4 ± 0.5	7.3 ± 3.2	–	–	0.5 ± 0.1	–	–
347	1239	Rehberg	87.8 ± 1.3	2.4 ± 0.0	5.9 ± 0.1	3.8 ± 1.5	–	–	0.3 ± 0.0	–	–
402	1290	Trifels	86.7 ± 1.6	3.0 ± 0.8	6.6 ± 0.3	3.5 ± 2.1	–	–	0.3 ± 0.0	–	–
453	1336	Trifels	82.3 ± 1.7	4.3 ± 0.6	9.4 ± 0.4	3.0 ± 1.8	0.8 ± 0.0	–	0.3 ± 0.1	–	–
497	1376	Annweiler	73.3 ± 3.0	4.8 ± 0.4	11.1 ± 0.6	7.8 ± 3.9	2.1 ± 0.0	–	0.9 ± 0.1	–	–
508	1386	Annweiler	70.6 ± 2.8	6.9 ± 1.1	13.8 ± 0.5	8.3 ± 4.5	–	–	0.5 ± 0.1	–	–
540	1414	Anté-Annweiler	66.4 ± 4.0	4.4 ± 0.9	10.7 ± 0.7	13.1 ± 6.0	4.2 ± 0.5	–	1.4 ± 0.1	–	–
Rothbach	Quarry	Karlstal	82.8 ± 0.5	7.8 ± 0.2	7.1 ± 0.2	1.8 ± 0.5	–	–	0.4 ± 0.2	–	–
Adamswiller	Quarry	Voltzia	71.8 ± 0.6	10.4 ± 0.2	11.8 ± 0.5	3.7 ± 1.0	–	–	0.7 ± 0.2	–	1.7 ± 0.2
Bust	Quarry	Voltzia	67.4 ± 1.0	10.4 ± 0.2	13.5 ± 0.5	4.0 ± 1.0	0.5 ± 0.1	–	0.5 ± 0.1	3.6 ± 0.5	–

straightforward in this case study because of the high quality of the core logs in the Bundsandstein. Despite not having descriptions of joint roughness, we feel confident that our assessments using discontinuity type, infilling type, and infilling thickness provide a suitable basis for assessing the joint condition. For example, discontinuities identified as faults can be assumed to have smooth to slickensided surfaces, resulting in a condition assessment of fair if they have no infilling, or very poor if they have thick (> 2 mm), clayey infilling. Discontinuities identified as joints can be assumed to have rough to smooth surfaces, resulting in a condition assessment of very good if they have no infilling, or very poor if they have thick (> 2 mm), clayey infilling.

The determination of the rock mass structure requires the selection of the scale at which the rock mass assessment is conducted. For example, [Villeneuve et al. \(2018\)](#) assessed the rock mass strength and elastic modulus of the granite underlying the Bundsandstein at the borehole scale. These authors demonstrated that the rock mass is so densely fractured in some intervals that the intact rock parameters are not appropriate. [Villeneuve et al. \(2018\)](#) suggested a range of 7–10 fractures per metre as the cut-off fracture density to decide between using the intact rock failure criterion (Eq. (1)) and using the rock mass failure criterion (Eq. (4)). In the present case study we derive the rock mass parameters at the reservoir scale (tens of metres). Based on the

recommendations of [Schultz \(1996\)](#), we use a block size to reservoir scale ratio of 5–10 as the cutoff for using rock mass strength and elastic modulus. We use fracture densities of 1 fracture per metre and 2 fractures per metre to differentiate between massive and blocky, and blocky and very blocky, respectively. In accordance with the reasoning detailed in [Villeneuve et al. \(2018\)](#), the cut-off between intact and rock mass failure criteria corresponds to approximately 2 fractures per metre.

3. Laboratory testing

3.1. Uniaxial compressive strength experiments

Representative uniaxial stress-strain curves for the dry Buntsandstein samples are shown in Fig. 4a. These stress-strain curves (Fig. 4a) are typical of those for brittle rock in compression (e.g., [Hoek and Bieniawski, 1965; Brace et al., 1966; Scholz, 1968](#)). The maximum axial stress obtained during the experiment is the uniaxial compressive strength, C_o (as labelled for one of the dry curves in Fig. 4a). Representative uniaxial stress-strain curves for a dry and wet sample of sample 100 are shown in Fig. 4b. These curves show that the uniaxial compressive strength is lower when the sample is wet. In the example

Table 2

Average connected porosity, average grain diameter, specific surface area, average dry and wet P-wave velocity, and average permeability for each of the twelve sandstones sampled from exploration well EPS-1 at the Soultz-sous-Forêts geothermal site and the three quarry rocks. Physical property data taken from [Heap et al. \(2017\)](#). Elastic wave velocities were measured at room pressure and permeabilities were measured under a confining pressure of 1 MPa. Grain size data for Rothbach and Adamswiller sandstone from [Louis et al. \(2005, 2009\)](#) and [David et al. \(1994\)](#), respectively.

Box number	Depth (m)	Unit	Average connected porosity	Average grain diameter (μm)	Specific surface area (m^2/kg)	Average dry P-wave velocity (km/s)	Average wet P-wave velocity (km/s)	Average permeability (m^2)
84	1008	Voltzia	0.096	142	1442	3.7	4.4	2.82×10^{-18}
100	1022	Intermédiaires	0.065	306	665	3.6	4.6	6.45×10^{-18}
157	1069	Karlstal	0.117	424	204	3.4	4.3	1.33×10^{-16}
198	1107	Karlstal	0.097	192	1485	3.2	4.4	7.95×10^{-17}
248	1151	Karlstal	0.144	294	1175	3.1	4.1	5.24×10^{-15}
299	1197	Rehberg	0.130	332	1888	3.4	4.1	1.15×10^{-17}
347	1239	Rehberg	0.185	367	1098	2.9	3.8	4.66×10^{-15}
402	1290	Trifels	0.131	259	1349	3.1	4.1	2.37×10^{-16}
453	1336	Trifels	0.189	361	1174	2.7	3.7	9.06×10^{-15}
497	1376	Annweiler	0.034	291	2024	4.1	5.1	2.08×10^{-18}
508	1386	Annweiler	0.082	199	2777	3.4	4.4	2.12×10^{-18}
540	1414	Anté-Annweiler	0.075	379	6170	2.9	4.2	7.89×10^{-18}
Rothbach	Quarry	Karlstal	0.191	100-150 (low-porosity layers) 200-250 (high-porosity layers)	–	3.4	3.9	6.94×10^{-14}
Adamswiller	Quarry	Voltzia	0.253	120	–	2.3	3.0	3.54×10^{-13}
Bust	Quarry	Voltzia	0.192	–	–	2.8	3.2	4.82×10^{-14}

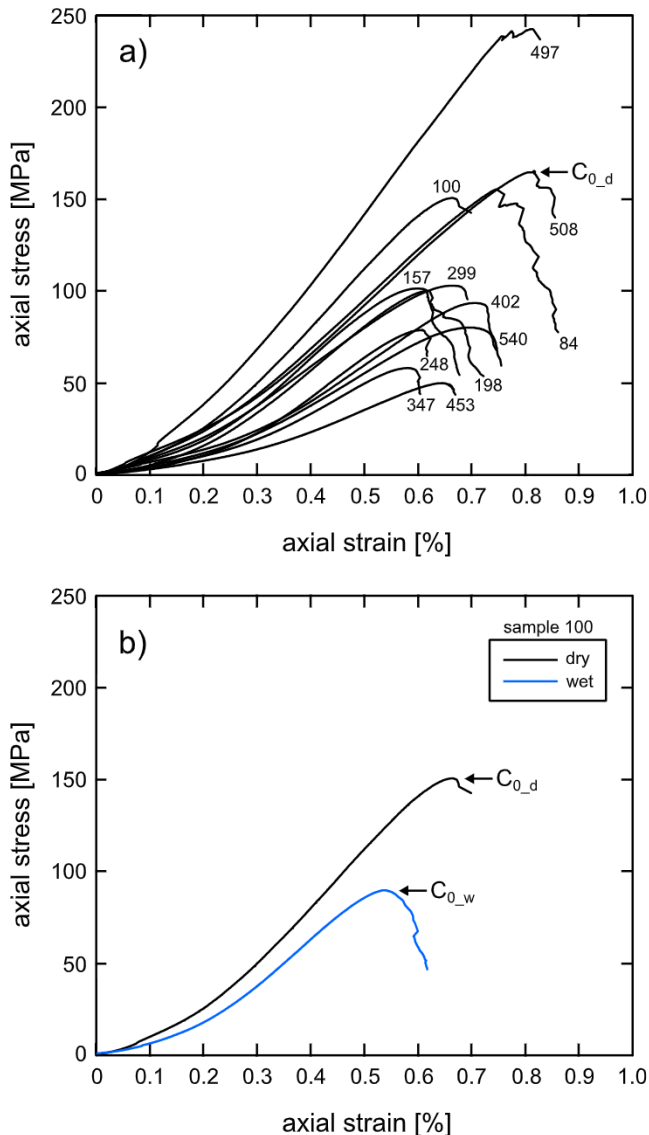


Fig. 4. (a) Representative dry uniaxial stress-strain curves for each of the twelve sandstones sampled from exploration well EPS-1 at Soultz-sous-Forêts. Number next to each curve indicates the box number (see Table 3). The dry uniaxial compressive strength, C_{0_d} , is labelled for one of the curves. (b) Representative dry (black curve) and wet (blue curve) uniaxial stress-strain curves for samples taken from box number 100 (see Table 3). The dry uniaxial compressive strength, C_{0_d} , and the wet uniaxial compressive strength, C_{0_w} , are labelled on the corresponding curves. (For interpretation of the references to colour in this figure legend, the reader is referred to the web version of this article).

shown in Fig. 4b, the dry strength, C_{0_d} , was 150.8 MPa and the wet strength, C_{0_w} , was 89.9 MPa. These representative curves also show that the slope of the stress-strain curve in the elastic region (i.e. the elastic modulus) and the axial strain at macroscopic failure are lower when the sample is wet (Fig. 4b).

Dry (white circles) and wet (blue squares) uniaxial compressive strengths (C_{0_d} and C_{0_w} , respectively) and elastic moduli (E_{i_d} and E_{i_w} , respectively) are plotted as a function of connected porosity in Fig. 5a and b, respectively (data available in Table 3). These data show that the strength (Fig. 5a) and elastic modulus (Fig. 5b) of the Buntsandstein samples studied here both decrease as the connected porosity is increased. For example, the dry strength and dry elastic modulus of the Buntsandstein samples tested herein range from ~50 MPa and ~10 GPa, respectively, at a porosity of ~0.25 up to ~250 MPa and

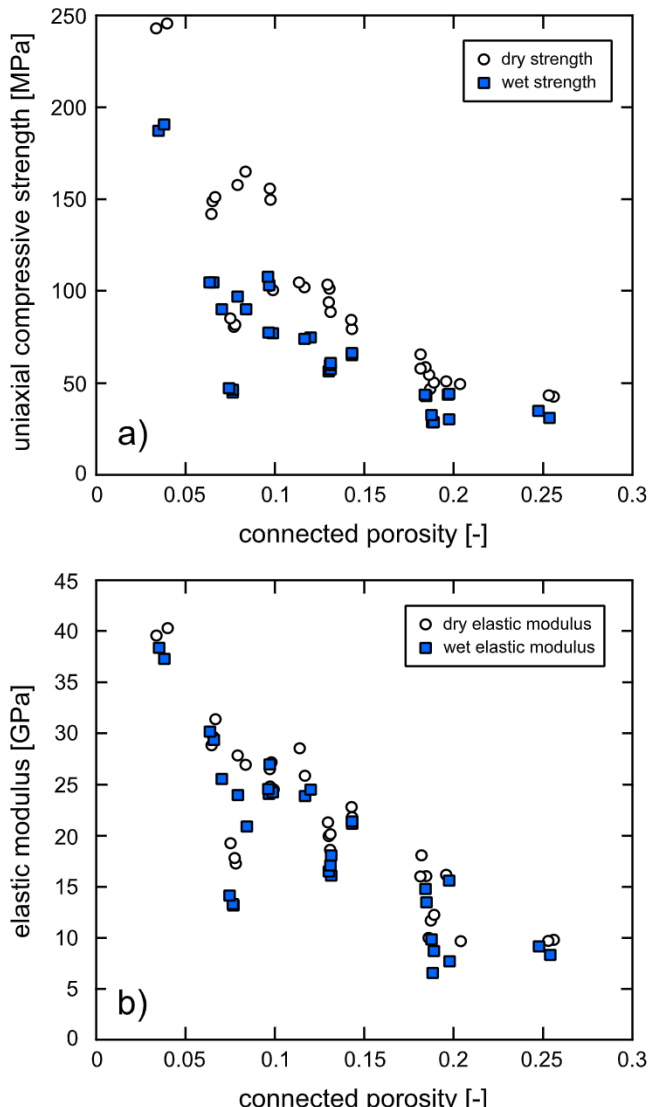


Fig. 5. (a) Dry (white circles) and wet (blue squares) uniaxial compressive strength for the twelve sandstones sampled from exploration well EPS-1 at Soultz-sous-Forêts and the three quarry rocks as a function of connected porosity. (b) Dry (white circles) and wet (blue squares) elastic modulus for the twelve sandstones sampled from exploration well EPS-1 at Soultz-sous-Forêts and the three quarry rocks as a function of connected porosity. (For interpretation of the references to colour in this figure legend, the reader is referred to the web version of this article).

~40 GPa, respectively, at a porosity of ~0.04 (Fig. 5a and b). These data also show that the wet strength and wet elastic modulus of the sandstones are systematically lower than the dry strength and dry elastic modulus across the entire tested porosity range (Fig. 5a and b).

The ratios of wet to dry strength are plotted as a function of connected porosity and clay content in Fig. 6a and b, respectively. These data show that the ratio of wet to dry strength varies from ~0.55 to ~0.84 for the rocks tested herein (Fig. 6). Fig. 6a shows that the observed water-weakening does not appear to depend on the connected porosity. However, although there is some scatter in the data, there is a trend of increasing water-weakening as clay content is increased (Fig. 6b). Indeed, the sample that contains the most clay (13.1 wt.%; sample 540) has the lowest ratio of wet to dry strength, and the sample containing the least clay (1.8 wt.%; Rothbach sandstone) has the highest ratio of wet to dry strength (Fig. 6b). The ratios of wet to dry elastic modulus are plotted as a function of connected porosity and clay content in Fig. 7a and b, respectively. These data show that the ratio of

Table 3

Summary of the dry and wet uniaxial compressive strength experiments performed on the twelve sandstones sampled from exploration well EPS-1 at the Soultz-sous-Forets geothermal site and the three quarry rocks. Also included are the connected porosity, average grain diameter, and clay content (average grain diameter and clay content taken from Heap et al., 2017).

Box number	Depth (m)	Unit	Connected porosity	Average grain diameter (μm)	Clay content (wt.%)	Dry UCS (C_{o-d}) (MPa)	Wet UCS (C_{o-w}) (MPa)	Elastic modulus (GPa)
84	1008	Voltzia	0.098	142	6.0	149.3	–	27.2
84	1008	Voltzia	0.097	142	6.0	155.4	–	26.6
84	1008	Voltzia	0.096	142	6.0	–	107.4	24.6
84	1008	Voltzia	0.097	142	6.0	–	102.8	27.0
100	1022	Intermédiaires	0.067	306	5.0	150.7	–	31.4
100	1022	Intermédiaires	0.065	306	5.0	148.5	–	29.7
100	1022	Intermédiaires	0.065	306	5.0	141.7	–	28.9
100	1022	Intermédiaires	0.070	306	5.0	–	89.9	25.6
100	1022	Intermédiaires	0.066	306	5.0	–	104.2	29.4
100	1022	Intermédiaires	0.064	306	5.0	–	104.4	30.2
157	1069	Karlstal	0.117	424	2.0	101.6	–	25.9
157	1069	Karlstal	0.114	424	2.0	104.3	–	28.6
157	1069	Karlstal	0.117	424	2.0	–	73.6	23.9
157	1069	Karlstal	0.120	424	2.0	–	74.6	24.5
198	1107	Karlstal	0.099	192	3.2	100.2	–	24.5
198	1107	Karlstal	0.097	192	3.2	102.6	–	24.8
198	1107	Karlstal	0.097	192	3.2	–	76.8	24.3
198	1107	Karlstal	0.099	192	3.2	–	77.0	24.1
248	1151	Karlstal	0.143	294	2.8	79.0	–	21.8
248	1151	Karlstal	0.143	294	2.8	84.1	–	22.8
248	1151	Karlstal	0.143	294	2.8	–	66.1	21.4
248	1151	Karlstal	0.143	294	2.8	–	64.9	21.2
299	1197	Rehberg	0.130	332	7.3	103.1	–	21.3
299	1197	Rehberg	0.131	332	7.3	101.1	–	18.6
299	1197	Rehberg	0.130	332	7.3	–	55.9	16.5
299	1197	Rehberg	0.131	332	7.3	–	57.0	16.1
347	1239	Rehberg	0.185	367	3.8	58.2	–	16.1
347	1239	Rehberg	0.182	367	3.8	57.4	–	16.0
347	1239	Rehberg	0.184	367	3.8	–	43.3	14.8
347	1239	Rehberg	0.185	367	3.8	–	42.4	13.5
402	1290	Trifels	0.130	259	3.5	93.6	–	19.9
402	1290	Trifels	0.131	259	3.5	88.2	–	20.1
402	1290	Trifels	0.131	259	3.5	–	59.5	17.1
402	1290	Trifels	0.131	259	3.5	–	60.5	18.1
453	1336	Trifels	0.189	361	3.0	50.0	–	12.3
453	1336	Trifels	0.187	361	3.0	46.6	–	11.7
453	1336	Trifels	0.188	361	3.0	–	32.3	9.9
453	1336	Trifels	0.189	361	3.0	–	28.2	8.7
497	1376	Annweiler	0.034	291	7.8	242.7	–	39.6
497	1376	Annweiler	0.040	291	7.8	245.2	–	40.3
497	1376	Annweiler	0.038	291	7.8	–	190.4	37.3
497	1376	Annweiler	0.035	291	7.8	–	187.1	38.4
508	1386	Annweiler	0.084	199	8.3	164.7	–	27.0
508	1386	Annweiler	0.079	199	8.3	157.3	–	27.9
508	1386	Annweiler	0.079	199	8.3	–	96.7	24.0
508	1386	Annweiler	0.084	199	8.3	–	89.7	20.9
540	1414	Anté-Annweiler	0.077	379	13.1	80.3	–	17.8
540	1414	Anté-Annweiler	0.075	379	13.1	84.7	–	19.3
540	1414	Anté-Annweiler	0.078	379	13.1	81.3	–	17.3
540	1414	Anté-Annweiler	0.077	379	13.1	–	44.4	13.2
540	1414	Anté-Annweiler	0.075	379	13.1	–	47.0	14.2
540	1414	Anté-Annweiler	0.076	379	13.1	–	45.9	13.4
Bust	Quarry	Voltzia	0.204	–	4.0	49.1	–	9.7
Bust	Quarry	Voltzia	0.186	–	4.0	54.0	–	10.0
Bust	Quarry	Voltzia	0.198	–	4.0	–	29.9	7.7
Bust	Quarry	Voltzia	0.188	–	4.0	–	28.5	6.6
Adamswiller	Quarry	Voltzia	0.253	120	3.7	42.8	–	9.7
Adamswiller	Quarry	Voltzia	0.256	120	3.7	42.1	–	9.8
Adamswiller	Quarry	Voltzia	0.254	120	3.7	–	30.8	8.3
Adamswiller	Quarry	Voltzia	0.248	120	3.7	–	34.5	9.2
Rothbach	Quarry	Karlstal	0.196	100-250	1.8	50.5	–	16.2
Rothbach	Quarry	Karlstal	0.182	100-250	1.8	65.1	–	18.1
Rothbach	Quarry	Karlstal	0.197	100-250	1.8	–	43.2	15.6
Rothbach	Quarry	Karlstal	0.198	100-250	1.8	–	43.9	15.6

wet to dry elastic modulus varies from ~0.74 to ~1.00 for the rocks tested herein (Fig. 7). The ratio of wet to dry elastic modulus does not appear to depend on either connected porosity (Fig. 7a) or clay content (Fig. 7b).

3.2. Triaxial compressive strength experiments

The stress-strain curves for the dry and wet triaxial experiments (on samples from sample 347) are shown in Fig. 8a and b, respectively. The

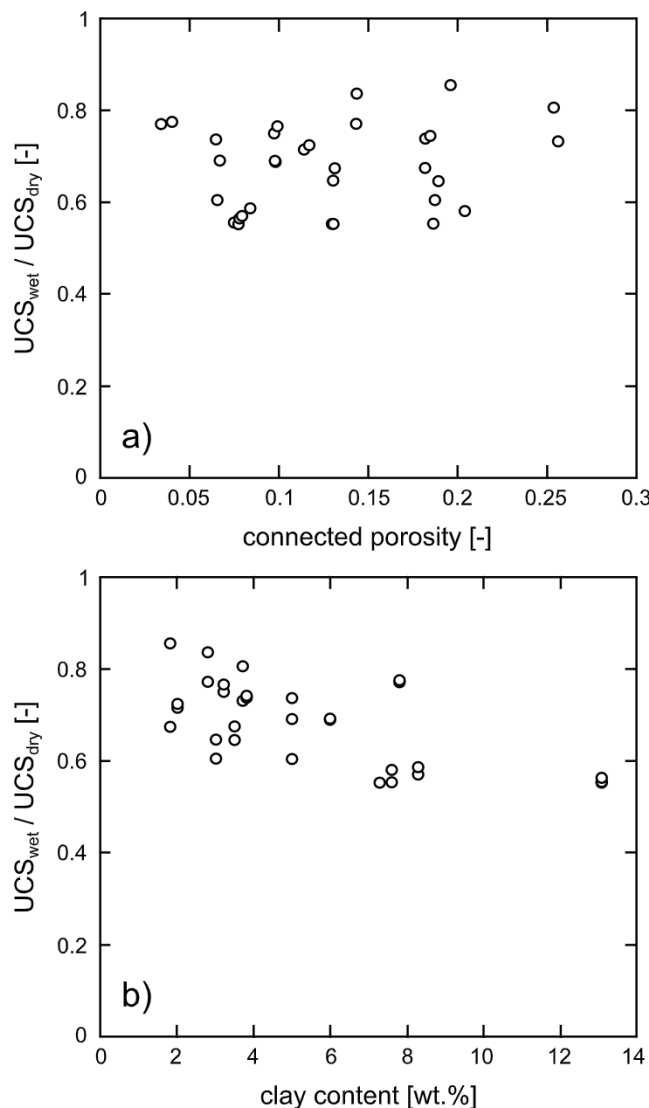


Fig. 6. (a) The ratio of wet to dry uniaxial compressive strength for the twelve sandstones sampled from exploration well EPS-1 at Soultz-sous-Forêts and the three quarry rocks as a function of connected porosity. (b) The ratio of wet to dry uniaxial compressive strength for the twelve sandstones sampled from exploration well EPS-1 at Soultz-sous-Forêts and the three quarry rocks as a function of clay content (clay content is the wt.% of muscovite/illite-smectite; Table 1).

sandstone is brittle over the tested pressure range and failure (marked by a stress drop in the stress-strain data; Fig. 8) was manifest as a through-going shear fracture. These data show that the dry (Fig. 8a) and wet (Fig. 8b) strength increases as the effective pressure is increased, in accordance with many experimental studies on sandstones in the brittle field (e.g., Wong et al., 1997; Baud et al., 2000; Bésuelle et al., 2003). For example, the dry strength was increased from ~ 58 MPa at an effective pressure of 0 MPa to ~ 141 MPa at an effective pressure of 15 MPa (Fig. 8a) (data available in Table 4). Our triaxial experiments also show that sample 347 is weaker when wet over the entire tested range of effective pressure (i.e. up to 15 MPa) (Fig. 8).

The triaxial data plotted in principal stress space (σ_1 as a function of σ_3 ; Fig. 9) show that the failure envelope for the wet samples (blue symbols in Fig. 9) is lower than the failure envelope for the dry samples (white symbols in Fig. 9). The fits to these data were provided by the Modified Cuckoo data fitting algorithm using basic (vertical) error summation, and relative (divided by the y-value of the curve fit) error type) in RocData (Rocscience Inc, 2017). These fits provide values of 19

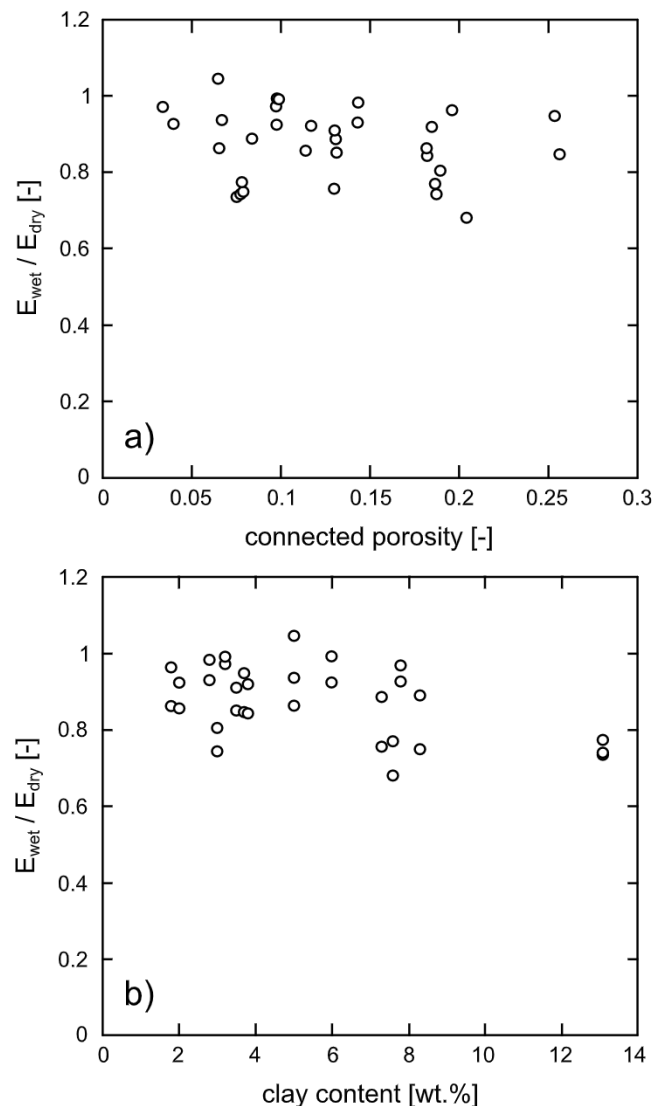


Fig. 7. (a) The ratio of wet to dry elastic modulus for the twelve sandstones sampled from exploration well EPS-1 at Soultz-sous-Forêts and the three quarry rocks as a function of connected porosity. (b) The ratio of wet to dry elastic modulus for the twelve sandstones sampled from exploration well EPS-1 at Soultz-sous-Forêts and the three quarry rocks as a function of clay content (clay content is the wt.% of muscovite/illite-smectite; Table 1).

(relative residuals 0.008) and 23 (relative residuals 0.012) for m_{i-d} and m_{i-w} , respectively. We note that the value for dry sandstone is within the range of m_i values typically associated with sandstone (17 ± 4 , as given in Hoek (2007)), whereas the value for wet sandstone is slightly higher than this range.

3.3. Geological Strength Index (GSI)

The rock mass descriptions, based on fracture frequency, infilling type, and infilling thickness are summarised in Table 5, along with their associated rock mass descriptions at the reservoir scale. Fig. 10 shows how the look-up chart from Marinos et al. (2005) was used to assess the GSI for two example intervals. For the depth interval 1365–1381 m the fracture density is 2.1 fractures per metre, and is therefore assessed as a “very blocky” (see Fig. 10) rock mass structure. The fractures are infilled with barite and minor calcite (both hard minerals that tend to seal fractures) with an infilling thickness averaging 2 mm. The surface condition of the fractures is therefore assessed as “good” (see Fig. 10) because barite and calcite are precipitated mineral infillings and will

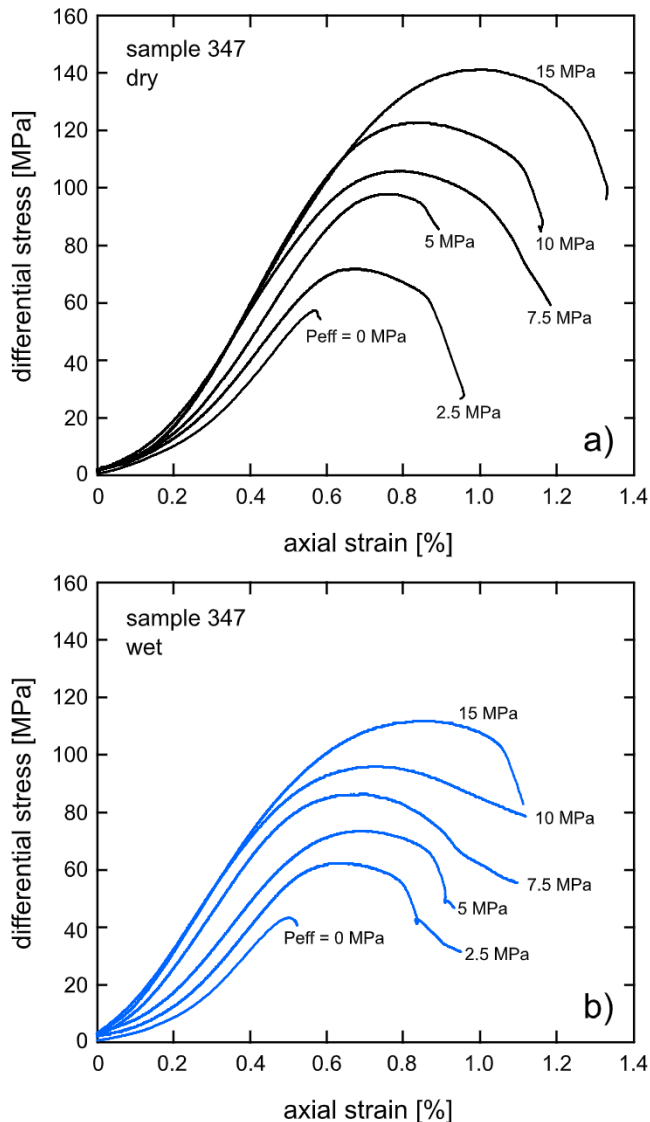


Fig. 8. (a) Dry triaxial stress-strain curves for samples taken from box number 347 (from the Rehberg unit; depth = 1239 m) deformed at different effective pressures (the effective pressure, P_{eff} , is indicated next to the curves). (b) Wet triaxial stress-strain curves for samples taken from box number 347 (from the Rehberg unit; depth = 1239 m) deformed at different effective pressures (the effective pressure, P_{eff} , is indicated next to the curves).

therefore contribute cohesive and frictional strength to the fracture. The combination of the two assessments results in a GSI range of 45–60. Since our analysis requires a single value of GSI, we use GSI = 55 for this interval (1365–1381 m) (Table 5). Similarly, the depth interval

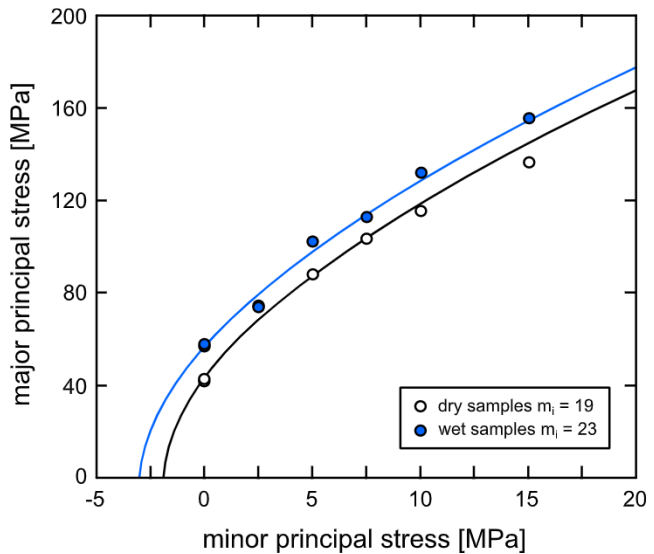


Fig. 9. Triaxial data for wet and dry Rehberg unit (depth = 1239 m) plotted in principal stress space with the intact Hoek-Brown failure criterion fits using Eq. (2) (for the dry data) and Eq. (3) (for the wet data). The best-fit m_i values for the dry and wet samples are given on the figure.

1012–1020 m has been assessed a “very blocky” (see Fig. 10) structure. Because of the presence of four faults within an 8 m thick interval, and an infilling thickness averaging 9 mm, the surface condition is assessed as “poor” (see Fig. 10). The combination results in a range of GSI of 25–40. Again, since our analysis requires a single value of GSI, we use GSI = 35 for this interval (1012–1020 m) (Table 5).

The majority of the rock mass in the Bundsandstein has a GSI of 100 (Table 5) because of its low fracture density (< 2 fractures per metre), with the resulting assessment of “massive” for the rock structure and the use of the intact Hoek-Brown failure criterion (Eq. (1)) to determine rock strength over these intervals. The intervals with GSI less than 100, of which there are five, are associated with highly fractured zones (e.g., the interval between depths 1151 and 1156 m has a fracture density of 2 discontinuities per metre) (Table 5). The five zones that are characterised by low values of GSI are located at depths of ~1012–1020, ~1151–1156, ~1205–1216, ~1347–1350, and ~1365–1381 m (Table 5). The zones with the lowest GSI (GSI = 35) are associated with highly fractured zones that contain fractures with a very thick average infilling (e.g., the interval between depths 1205 and 1216 m has an average infilling thickness of 11 mm; Table 5). The three zones with the lowest GSI (Table 5) were previously identified as the three main fractured zones within the EPS-1 core (Vernoux et al., 1995).

Table 4

Summary of the dry and wet triaxial compressive strength experiments performed on samples taken from box number 347 (from the Rehberg unit).

Sample	Connected porosity	Condition	Confining pressure (MPa)	Pore fluid pressure (MPa)	Effective pressure (MPa)	Peak differential stress (MPa)
347_12	0.181	Dry	2.5	0	2.5	71.8
347_8	0.179	Dry	5	0	5	97.7
347_13	0.177	Dry	7.5	0	7.5	105.8
347_9	0.178	Dry	10	0	10	122.5
347_11	0.181	Dry	15	0	15	141.1
347_23	0.179	Wet	12.5	10	2.5	62.3
347_14	0.180	Wet	15	10	5	73.4
347_17	0.177	Wet	17.5	10	7.5	86.3
347_16	0.177	Wet	20	10	10	95.9
347_18	0.179	Wet	25	10	15	111.8

Table 5
Summary of rock mass descriptions for Geological Strength Index (GSI) assessment, and the resulting intact and rock mass strength and elastic modulus for the wet and dry sandstone units. Wet and dry intact C_o and E_i are given as averages for the rock type associated with the rock mass interval. $S_{h\min}$ = minimum horizontal stress; UCS = uniaxial compressive strength; E_i = intact elastic modulus; E_{rm} = rock mass elastic modulus.

Logging Depth (m)	Fracture Density (m^{-1})	Structure Description at Reservoir Scale	Dominant Infilling	Infilling Thickness (mm)	Surface Condition Description	GSI for Eq. (5)	$S_{h\min}$ (MPa)	Strength	Elastic Modulus										
									Wet Samples $m_{t,w} = 23$			Dry Samples $m_{t,d} = 19$							
									Average Wet UCS	Intact Strength	Rock Mass Strength (MPa)	Average Dry UCS	Intact Strength	Rock Mass Strength (MPa)					
1012	1020	2.3	very blocky	barite, calcite, organics, 4 faults	9	poor	35	27	13	105	221	30	152	261	31	26	2	27	2
1059	1117	0.8 0.9	massive	minor faults, barite, minor quartz, organics	2	good	100 100	28 29	14	100 76	216 188	147 102	257 209	28 24	28 24	30 26	30 26	30 26	
11151	1156	0.1 2.0	massive very blocky	4 faults barite	0 1	fair good	100 55	30 31	15	66 66	178 179	82 45	186 188	21 21	21 21	22 5	22 22	22 22	
1170	1205	0.3 1.6	massive blocky	minor faults, barite, minor quartz	0 6 11	fair poor	100 35	31 32	15	56 56	180 168	82 168	189 102	21 216	21 16	21 20	21 20	21 20	
1216	1291	3.2 0.4	very blocky	barite, minor calcite	0 0	good	100 100	33 34	16	43 60	150 181	58 91	162 210	218 210	14 18	14 18	16 20	16 20	
1298	1347	1.6 0.3	massive blocky	barite, minor calcite	0 1	good	100 100	35 35	17	30	131 131	48 48	162 152	32 9	14 9	14 9	16 12	16 12	
1347	1350	3.0 0.2	very blocky	6 faults barite, minor calcite	11 0	poor good	35 100	36 36	18	30 18	132 133	28 48	162 154	29 9	14 9	14 9	16 12	16 12	
1365	1381	2.1 0.2	massive very blocky	4 faults, barite, calcite	2 0	good fair	55 100	36 37	18	141 46	297 164	66 82	202 206	349 206	7 14	34 18	8 18	8 18	

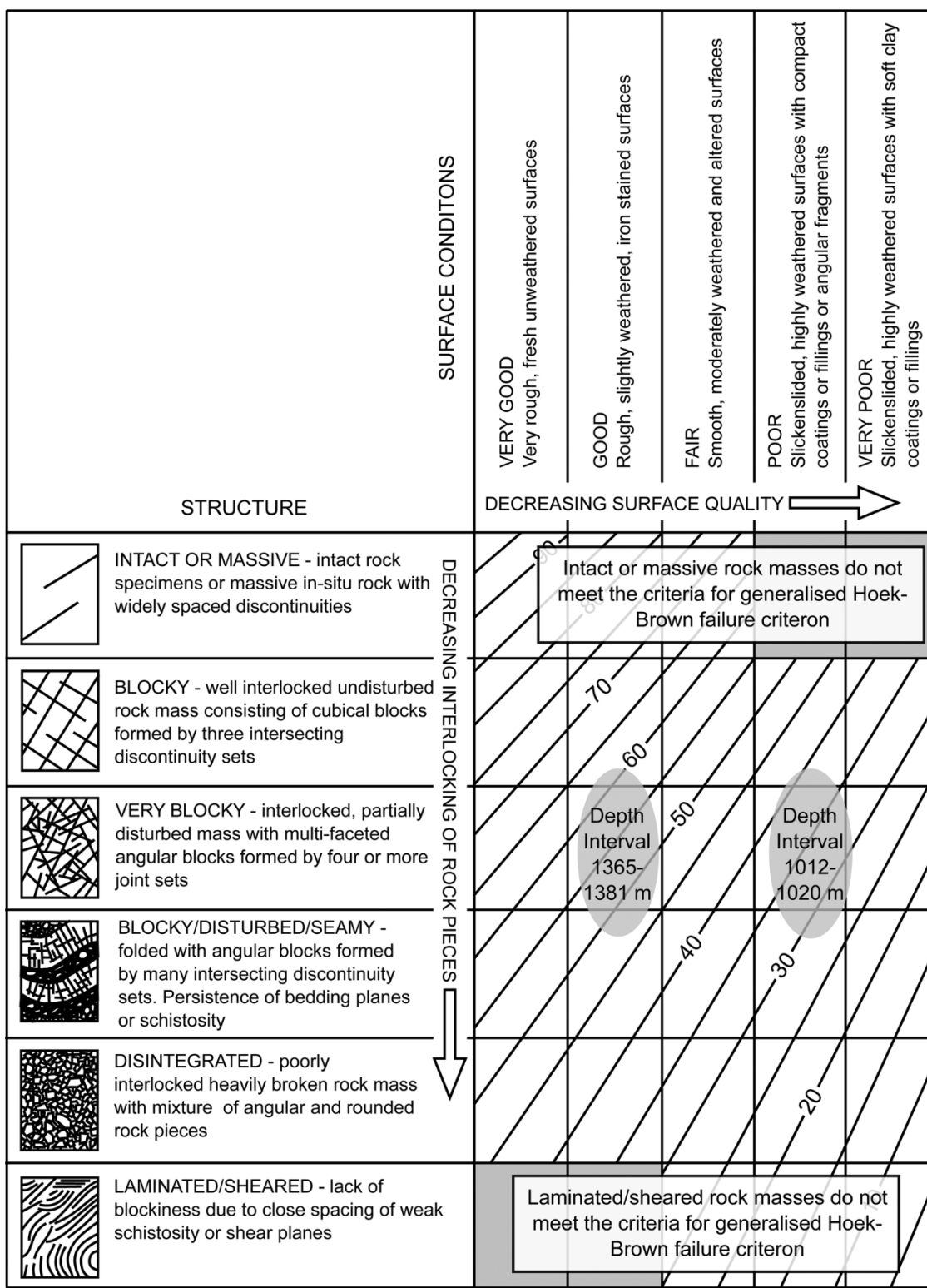


Fig. 10. Geological Strength Index (GSI) lookup chart (modified from Marinos et al., 2005) showing the assessed GSI values for two rock mass intervals (see text for details). See Table 5 for rock mass descriptions based on core logging. Note that the highest and lowest category should not be used for the generalised Hoek-Brown failure criterion (as indicated on the figure).

4. Reservoir-scale strength and elastic modulus for the Buntsandstein

The dry and wet intact and rock mass strength and elastic modulus, calculated using the reservoir scale GSI and Eqs. (1), (2), (3), (8), and (9) (for the strength) and Eqs. (13) and (14) (for the elastic modulus)

are given in Table 5. The fracture density with depth (Fig. 11a) is plotted alongside the dry and wet strength and elastic modulus in Fig. 11b and c, respectively. Fig. 11b and c clearly show the five zones for which the rock mass strength and rock mass elastic modulus is applicable (at depths of ~1012–1020, ~1151–1156, ~120–1216, ~1347–1350, and ~1365–1381 m; indicated by the black arrows in

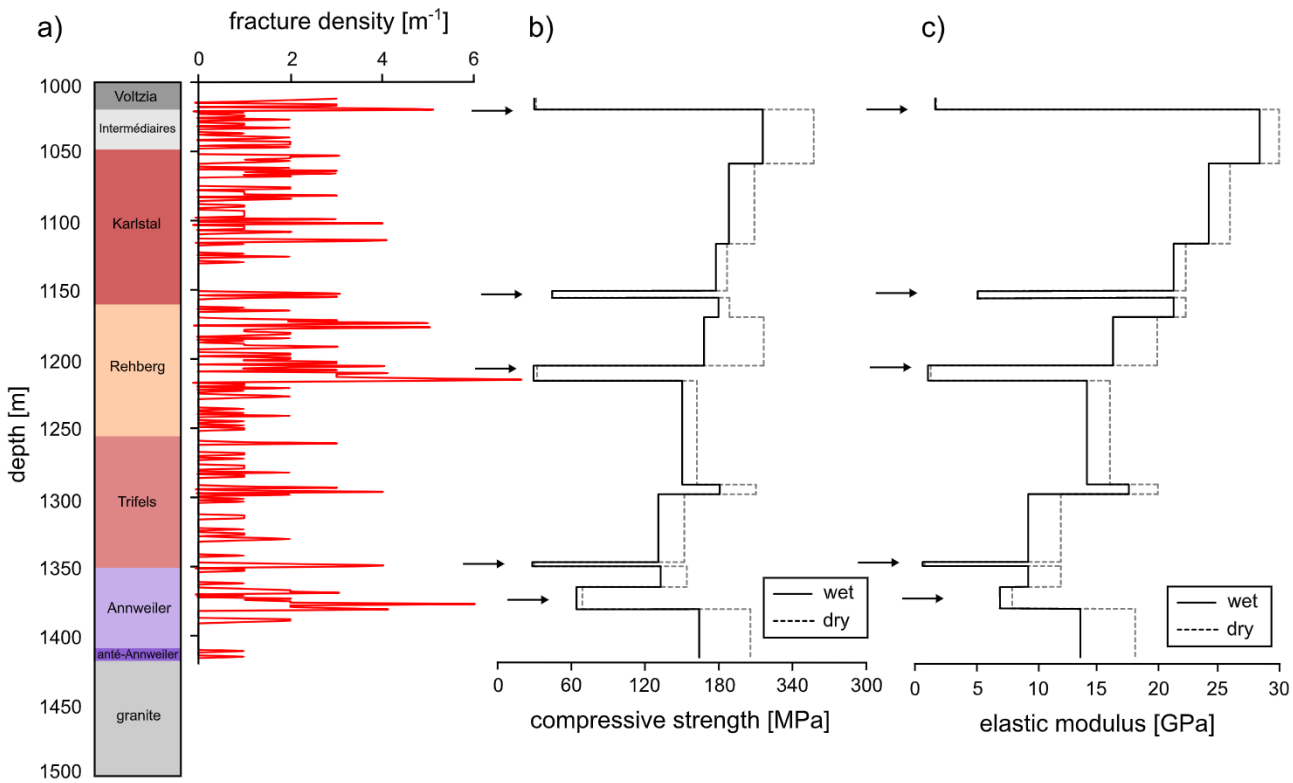


Fig. 11. (a) Stratigraphic column showing the units within the Buntsandstein from exploration well EPS-1 at Soultz-sous-Forêts next to the fracture density data for the core. (b) Wet (black line) and dry (grey dashed line) rock mass compressive strength for the Buntsandstein over the depth interval 1012–1416 m. (c) Wet (black line) and dry (grey dashed line) rock mass elastic modulus for the Buntsandstein over the depth interval 1012–1416 m. The black arrows indicate the five fractured zones.

Fig. 11, as opposed to those where the intact values of either property are appropriate. These zones are characterised by low values of strength (**Fig. 11b**) and elastic modulus (**Fig. 11c**). Apart from these five zones, the strength and elastic modulus of the rock mass is given by the intact strength and the intact elastic modulus ($\text{GSI} = 100$; **Table 5**). Excluding the rock at the interface between the granite and the sedimentary rocks (the *Anté-Annweiler*), which has relatively high values of strength and elastic modulus, the overall strength (**Fig. 11b**) and elastic modulus (**Fig. 11c**) of the Buntsandstein appears to decrease with depth; this is especially true for the elastic modulus (**Fig. 11c**).

We also note that, in the five zones where the strength and elastic modulus are described by the rock mass strength and elastic modulus, respectively, there is essentially no difference between the dry and wet values (**Fig. 11b** and c). In these zones, the strength and elastic modulus of the rock mass very much depends on the fractures present within the rock mass, rather than the condition (wet or dry) of the rock mass. However, in the depths characterised by the intact strength and elastic modulus, a large difference can be observed between the wet and dry values (**Fig. 11b** and c).

5. Discussion

5.1. Water-weakening in sandstones

Water-weakening in rocks can be the result of both mechanical and chemical processes. Mechanically, pressurised pore fluids typically weaken and embrittle rocks (e.g., [Paterson and Wong, 2005](#)). Chemically, rock can be weakened by subcritical crack growth processes (e.g., [Atkinson, 1984](#)) and the reduction of surface free energy (e.g., [Parks, 1984](#)). The mechanical effect can be expressed in terms of the effective pressure law, where the effective pressure equals the confining pressure minus the pore fluid pressure multiplied by a poroelastic constant. The

study of [Baud et al. \(2015\)](#) shows that this poroelastic constant is very close to unity for porous sandstone. As a result, we do not consider herein the mechanical influence of pore fluids on the strength of our sandstone samples.

Our deformation experiments have shown that sandstone is weaker in the presence of water (**Figs. 4–8**), in accordance with many published studies (e.g., [Rutter and Mainprice, 1978](#); [Bell, 1978](#); [Hadizadeh and Law, 1991](#); [Dyke and Dobereiner, 1991](#); [Hawkins and McConnell, 1992](#); [Kasim and Shakoor, 1996](#); [Zang et al., 1996](#); [Bell and Culshaw, 1998](#); [Baud et al., 2000](#); [Cuss et al., 2003](#); [Lin et al., 2005](#); [Vásárhelyi and Ván, 2006](#); [Demarco et al., 2007](#); [Shakoor and Barefield, 2009](#); [Nespereira et al., 2010](#); [Siedel et al., 2010](#); [Wasantha and Ranjith, 2014](#)). A handful of these studies highlight that the observed water-weakening in sandstones is related to their clay content. For example, [Hawkins and McConnell \(1992\)](#) found that the uniaxial compressive strength (UCS) of sandstone was reduced by 78% for clay-rich sandstones and by only 8% for siliceous sandstones in the presence of water. Although our data suggest that the water-weakening in sandstone does not depend on connected porosity (**Fig. 6a**), they do highlight that water-weakening may increase as clay content is increased (**Fig. 6b**). To better understand the role of connected porosity and clay content on water-weakening in sandstone, we plot ratios of wet to dry strength from numerous studies (data available in **Table 6**) alongside our new data (**Table 3**) as a function of porosity and clay content in **Fig. 12a** and b, respectively. **Fig. 12a** shows that there is no discernible trend between water-weakening in sandstone and porosity. However, **Fig. 12b** shows that, although there is some scatter in the data, water-weakening increases as clay content is increased. Indeed, the sample containing the highest clay content (~70%) has the lowest ratio of wet to dry strength (**Fig. 12b**).

To explore the reason for the reduction in strength in the presence of water we use the micromechanical model of [Sammis and Ashby \(1986\)](#).

Table 6

Published wet and dry uniaxial compressive strength data for sandstones. Rate in brackets for the Pennant sandstone experiments (Hadizadeh and Law, 1991) is the experimental strain rate. H & L = Hadizadeh and Law; H & M = Hawkins and McConnell; para = parallel to bedding; perp = perpendicular to bedding.

Sandstone	Porosity	Clay content (%)	Dry UCS (MPa)	Wet UCS (MPa)	UCS _{wet} / UCS _{dry}	Reference
Fell sandstone	0.111	–	33.2	19.1	0.58	Bell (1978)
Fell sandstone	0.127	–	51.9	31.0	0.60	Bell (1978)
Fell sandstone	0.115	–	73.7	43.3	0.59	Bell (1978)
Fell sandstone	0.117	–	79.1	53.5	0.68	Bell (1978)
Fell sandstone	0.205	–	38.1	21.6	0.57	Bell (1978)
Fell sandstone	0.096	–	108.9	98.6	0.91	Bell (1978)
Fell sandstone	0.095	–	88.7	70.2	0.79	Bell (1978)
Fell sandstone	0.104	–	90.2	71.2	0.79	Bell (1978)
Fell sandstone	0.095	–	89.9	63.4	0.71	Bell (1978)
Fell sandstone	0.094	–	51.1	33.5	0.66	Bell (1978)
Fell sandstone	0.099	–	59.0	38.2	0.65	Bell (1978)
Fell sandstone	0.101	–	91.7	62.7	0.68	Bell (1978)
Fell sandstone	0.092	–	92.4	60.9	0.66	Bell (1978)
Fell sandstone	0.072	–	112.4	97.2	0.87	Bell (1978)
Fell sandstone	0.071	–	53.9	29.6	0.55	Bell (1978)
Fell sandstone	0.076	–	75.2	62.0	0.82	Bell (1978)
Fell sandstone	0.096	–	60.2	37.3	0.62	Bell (1978)
Fell sandstone	0.101	–	52.3	30.6	0.59	Bell (1978)
Fell sandstone	0.091	–	77.2	43.1	0.56	Bell (1978)
Fell sandstone	0.078	–	55.7	42.7	0.77	Bell (1978)
Fell sandstone	0.081	–	93.1	43.9	0.47	Bell (1978)
Fell sandstone	0.069	–	107.2	98.4	0.92	Bell (1978)
Fell sandstone	0.065	–	95.8	64.9	0.68	Bell (1978)
Fell sandstone	0.087	–	80.5	50.8	0.63	Bell (1978)
Pennant sandstone ($10^{-2.0} \text{ s}^{-1}$)	0.025	25	257.3	143.5	0.56	Hadizadeh and Law (1991)
Pennant sandstone ($10^{-2.0} \text{ s}^{-1}$)	0.025	25	263.7	151.9	0.58	Hadizadeh and Law (1991)
Pennant sandstone ($10^{-2.2} \text{ s}^{-1}$)	0.025	25	268.3	141.3	0.53	Hadizadeh and Law (1991)
Pennant sandstone ($10^{-2.2} \text{ s}^{-1}$)	0.025	25	259.0	136.2	0.53	Hadizadeh and Law (1991)
Pennant sandstone ($10^{-2.4} \text{ s}^{-1}$)	0.025	25	263.1	162.4	0.62	Hadizadeh and Law (1991)
Pennant sandstone ($10^{-2.4} \text{ s}^{-1}$)	0.025	25	247.1	151.8	0.62	Hadizadeh and Law (1991)
Pennant sandstone ($10^{-2.4} \text{ s}^{-1}$)	0.025	25	272.9	157.3	0.58	Hadizadeh and Law (1991)
Pennant sandstone ($10^{-2.6} \text{ s}^{-1}$)	0.025	25	267.7	154.7	0.58	Hadizadeh and Law (1991)
Pennant sandstone ($10^{-2.6} \text{ s}^{-1}$)	0.025	25	274.1	161.0	0.59	Hadizadeh and Law (1991)
Pennant sandstone ($10^{-2.9} \text{ s}^{-1}$)	0.025	25	275.7	156.4	0.57	Hadizadeh and Law (1991)
Pennant sandstone ($10^{-3.3} \text{ s}^{-1}$)	0.025	25	278.5	162.6	0.58	Hadizadeh and Law (1991)
Pennant sandstone ($10^{-3.4} \text{ s}^{-1}$)	0.025	25	262.8	154.5	0.59	Hadizadeh and Law (1991)
Pennant sandstone ($10^{-3.5} \text{ s}^{-1}$)	0.025	25	253.5	159.1	0.63	Hadizadeh and Law (1991)
Pennant sandstone ($10^{-3.6} \text{ s}^{-1}$)	0.025	25	267.9	151.5	0.57	Hadizadeh and Law (1991)
Pennant sandstone ($10^{-4.0} \text{ s}^{-1}$)	0.025	25	257.2	148.0	0.58	Hadizadeh and Law (1991)
Pennant sandstone ($10^{-4.1} \text{ s}^{-1}$)	0.025	25	258.8	145.4	0.56	Hadizadeh and Law (1991)
Pennant sandstone ($10^{-4.5} \text{ s}^{-1}$)	0.025	25	246.5	143.6	0.58	Hadizadeh and Law (1991)
Pennant sandstone ($10^{-4.6} \text{ s}^{-1}$)	0.025	25	254.5	144.8	0.57	Hadizadeh and Law (1991)
Pennant sandstone ($10^{-4.8} \text{ s}^{-1}$)	0.025	25	265.9	146.9	0.55	Hadizadeh and Law (1991)
Pennant sandstone ($10^{-4.8} \text{ s}^{-1}$)	0.025	25	255.3	138.9	0.54	Hadizadeh and Law (1991)
Pennant sandstone ($10^{-4.8} \text{ s}^{-1}$)	0.025	25	244.7	138.8	0.57	Hadizadeh and Law (1991)
Pennant sandstone ($10^{-5.4} \text{ s}^{-1}$)	0.025	25	250.9	136.1	0.54	Hadizadeh and Law (1991)
Pennant sandstone ($10^{-5.5} \text{ s}^{-1}$)	0.025	25	252.5	132.7	0.53	Hadizadeh and Law (1991)
Pennant sandstone ($10^{-5.5} \text{ s}^{-1}$)	0.025	25	260.2	133.2	0.51	Hadizadeh and Law (1991)
Pennant sandstone ($10^{-6.2} \text{ s}^{-1}$)	0.025	25	240.1	131.3	0.55	Hadizadeh and Law (1991)
Pennant sandstone ($10^{-6.8} \text{ s}^{-1}$)	0.025	25	229.3	124.3	0.54	Hadizadeh and Law (1991)
Pennant sandstone ($10^{-6.8} \text{ s}^{-1}$)	0.025	25	221.7	118.4	0.53	Hadizadeh and Law (1991)
Pennant sandstone ($10^{-7.9} \text{ s}^{-1}$)	0.025	25	222.2	126.5	0.57	Hadizadeh and Law (1991)
Applecross	0.054	3.0	141.3	99.3	0.70	Hadizadeh and Law (1991)
Donegal Quartzite	0.013	0.0	237.9	184.0	0.77	Hadizadeh and Law (1991)
Basal Quartzite	0.006	0.0	247.0	202.1	0.82	Hadizadeh and Law (1991)
Brownstones	0.067	3.1	152.0	107.4	0.71	Hadizadeh and Law (1991)
Pilton (type A)	0.006	16.0	173.3	152.2	0.88	Hadizadeh and Law (1991)
Pilton (type B)	0.006	4.3	227.3	208.4	0.92	Hadizadeh and Law (1991)
Upper Cromhall	0.045	0.0	161.4	143.9	0.89	Hadizadeh and Law (1991)
Millstone Grit A	0.118	13.9	59.3	39.6	0.67	Hadizadeh and Law (1991)
Millstone Grit B	0.116	12.0	49.0	40.2	0.82	Hadizadeh and Law (1991)
Millstone Grit C	–	12.7	123.4	72.1	0.58	Hadizadeh and Law (1991)
Millstone Grit D	–	9.2	127.5	98.6	0.77	Hadizadeh and Law (1991)
Holcomb Brook Grit A	0.1	15.2	119.1	49.0	0.41	Hadizadeh and Law (1991)
Holcomb Brook Grit B	0.103	16.7	108.1	48.6	0.45	Hadizadeh and Law (1991)
Siliceous Sandstone	0.012	3.0	198.4	182.2	0.92	Hadizadeh and Law (1991)
Elland Flags	0.124	12.6	59.9	31.4	0.52	Hadizadeh and Law (1991)
Thornhill Rock A	0.12	5.9	89.9	38.4	0.43	Hadizadeh and Law (1991)
Thornhill Rock B	0.12	14.4	91.8	46.7	0.51	Hadizadeh and Law (1991)
Middle Coal Measures	0.13	9.4	37.1	25.3	0.68	Hadizadeh and Law (1991)
Crackington Formation	–	15.3	298.2	232.3	0.78	Hadizadeh and Law (1991)
Pennant A	0.073	2.3	114.2	50.0	0.44	Hadizadeh and Law (1991)
Pennant B	0.069	7.9	106.2	52.6	0.50	Hadizadeh and Law (1991)

(continued on next page)

Table 6 (continued)

Sandstone	Porosity	Clay content (%)	Dry UCS (MPa)	Wet UCS (MPa)	UCS _{wet} / UCS _{dry}	Reference
Pennant C	0.082	2.0	103.4	47.0	0.46	Hadizadeh and Law (1991)
Annan Sandstone	0.135	6.3	66.3	43.6	0.66	Hadizadeh and Law (1991)
Penrith A	0.075	1.9	66.0	53.1	0.81	Hadizadeh and Law (1991)
Penrith B	0.122	2.2	34.8	29.4	0.85	Hadizadeh and Law (1991)
Penrith C	0.054	0.7	82.0	72.8	0.89	Hadizadeh and Law (1991)
Penrith D	0.046	0.1	101.2	87.9	0.87	Hadizadeh and Law (1991)
Penrith E	0.115	6.2	59.7	40.8	0.68	Hadizadeh and Law (1991)
Redcliffe	–	3.2	36.1	22.4	0.62	Hadizadeh and Law (1991)
Midford Sands	0.156	1.7	23.2	14.6	0.63	Hadizadeh and Law (1991)
Ardingly Sandstone A	0.19	4.9	42.2	36.9	0.87	Hadizadeh and Law (1991)
Ardingly Sandstone B	0.173	8.9	53.4	47.6	0.89	Hadizadeh and Law (1991)
Ashdown Sandstone	0.201	0.4	30.6	32.3	1.06	Hadizadeh and Law (1991)
Greensand A	0.383	50.5	10.5	2.3	0.22	Hadizadeh and Law (1991)
Greensand A Dogger	0.173	16.9	74.5	46.7	0.63	Hadizadeh and Law (1991)
Chatsworth Grit	0.146	–	39.2	24.3	0.62	Bell (1995)
Sherwood Sandstone	0.257	–	11.6	4.8	0.41	Bell (1995)
Keuper Waterstone	0.101	–	42.0	28.6	0.68	Bell (1995)
Bronllwyn Grit	0.018	–	197.5	190.7	0.97	Bell (1995)
Sneinton Formation sandstone	0.163	11.0	23.7	14.1	0.60	Bell and Culshaw (1998)
Sneinton Formation sandstone	0.178	14.0	26.1	16.2	0.62	Bell and Culshaw (1998)
Sneinton Formation sandstone	0.18	6.0	25.2	16.8	0.67	Bell and Culshaw (1998)
Sneinton Formation sandstone	0.182	7.0	27.6	19.6	0.71	Bell and Culshaw (1998)
Sneinton Formation sandstone	0.167	4.0	26.4	20.1	0.76	Bell and Culshaw (1998)
Sneinton Formation sandstone	0.163	10.0	32.5	17.6	0.54	Bell and Culshaw (1998)
Sneinton Formation sandstone	0.19	5.0	24.4	13.7	0.56	Bell and Culshaw (1998)
Sneinton Formation sandstone	0.186	12.0	28.0	20.5	0.73	Bell and Culshaw (1998)
Sneinton Formation sandstone	0.166	6.0	17.4	10.7	0.62	Bell and Culshaw (1998)
Sneinton Formation sandstone	0.187	6.0	39.8	25.6	0.64	Bell and Culshaw (1998)
Sneinton Formation sandstone	0.181	12.0	30.9	24.9	0.81	Bell and Culshaw (1998)
Penrith sandstone	0.28	5.0	28.4	9.37	0.33	Cuss et al. (2003)
Darley Dale sandstone	0.135	6.0	44.4	37.7	0.85	Cuss et al. (2003)
Tennessee (Crab Orchard) sandstone	0.075	10.0	89.9	69.4	0.77	Cuss et al. (2003)
Tertiary sandstone (Taiwan) (WGS1)	0.174	21.3	34.1	25.4	0.75	Lin et al. (2005)
Tertiary sandstone (Taiwan) (WGS2)	0.167	69.6	47.5	6.7	0.14	Lin et al. (2005)
Tertiary sandstone (Taiwan) (MS1)	0.115	43.1	48.5	28.9	0.60	Lin et al. (2005)
Tertiary sandstone (Taiwan) (MS2)	0.141	21.5	37.1	28.3	0.76	Lin et al. (2005)
Tertiary sandstone (Taiwan) (MS3)	0.131	41.3	82.7	43.3	0.52	Lin et al. (2005)
Tertiary sandstone (Taiwan) (TL1)	0.131	58.1	68.7	23.2	0.34	Lin et al. (2005)
Tertiary sandstone (Taiwan) (TL2)	0.128	42.7	77.5	44.2	0.57	Lin et al. (2005)
Tertiary sandstone (Taiwan) (ST)	0.182	50.6	38.4	7.8	0.20	Lin et al. (2005)
Tertiary sandstone (Taiwan) (NK)	0.148	66.4	86.0	43.2	0.50	Lin et al. (2005)
Tertiary sandstone (Taiwan) (TK)	0.128	67.7	69.0	29.4	0.43	Lin et al. (2005)
Tertiary sandstone (Taiwan) (SFG1)	0.246	30.2	14.5	12.2	0.84	Lin et al. (2005)
Tertiary sandstone (Taiwan) (SFG2)	0.169	48.6	46.4	19.9	0.43	Lin et al. (2005)
Tertiary sandstone (Taiwan) (CL)	0.207	50.4	19.9	3.1	0.16	Lin et al. (2005)
Balatonrendes sandstone (Hungary)	0.042	–	45.7	35.0	0.77	Vásárhelyi and Ván (2006)
Cserkút sandstone (Hungary)	0.018	–	78.6	61.4	0.78	Vásárhelyi and Ván (2006)
Pilisborosjenő sandstone (Hungary)	0.135	–	20.4	17.7	0.87	Vásárhelyi and Ván (2006)
Vác sandstone (Hungary)	0.121	–	33.8	25.2	0.75	Vásárhelyi and Ván (2006)
Bad Bentheim (perp)	0.233	6	50.4	49.4	0.98	Demarco et al. (2007)
Bad Bentheim (para)	0.233	6	50.2	49.5	0.99	Demarco et al. (2007)
Bebertal (perp)	0.09	1	92.8	58.2	0.63	Demarco et al. (2007)
Bebertal (para)	0.09	1	75.8	42.2	0.56	Demarco et al. (2007)
Obernkirchen (perp)	0.264	6	64.4	55.2	0.86	Demarco et al. (2007)
Obernkirchen (para)	0.264	6	55.6	48.0	0.86	Demarco et al. (2007)
Sander (perp)	0.147	5	70.7	37.5	0.53	Demarco et al. (2007)
Sander (para)	0.147	5	64.0	32.7	0.51	Demarco et al. (2007)
Schleeriethe (perp)	0.142	2	84.4	43.5	0.52	Demarco et al. (2007)
Schleeriethe (para)	0.142	2	69.3	34.3	0.50	Demarco et al. (2007)
Tambach (perp)	0.084	1	204.6	194.6	0.95	Demarco et al. (2007)
Tambach (para)	0.084	1	179.4	140.0	0.78	Demarco et al. (2007)
Weser grau (perp)	0.094	1	164.8	136.5	0.83	Demarco et al. (2007)
Weser grau (para)	0.094	1	153.4	133.2	0.87	Demarco et al. (2007)
Weser rot (perp)	0.063	2	145.5	94.9	0.65	Demarco et al. (2007)
Weser rot (para)	0.063	2	154.0	104.8	0.68	Demarco et al. (2007)
Los Alambres sandstone (Salamanca, Spain)	0.145	–	36.0	19.7	0.55	Nespereira et al. (2010)
Matagrillos sandstone (Salamanca, Spain)	0.119	–	23.0	15.8	0.69	Nespereira et al. (2010)
Arapiles A-1-1 sandstone (Salamanca, Spain)	0.103	–	58.1	42.1	0.72	Nespereira et al. (2010)
Arapiles A-2-1 sandstone (Salamanca, Spain)	0.133	–	177.6	162.9	0.92	Nespereira et al. (2010)
Arapiles A-2-2 sandstone (Salamanca, Spain)	0.088	–	119.4	109.1	0.91	Nespereira et al. (2010)
Cotta-type Elbe sandstone (LG XI)	0.199	2.7	40.5	31.7	0.78	Siedel et al. (2010)
Cotta-type Elbe sandstone (LG 12)	0.239	3.3	29.4	20.6	0.70	Siedel et al. (2010)
Cotta-type Elbe sandstone (LG 14)	0.274	2.1	30.5	20.3	0.67	Siedel et al. (2010)
Cotta-type Elbe sandstone (LG 15)	0.267	2.4	31.6	24.1	0.76	Siedel et al. (2010)
Cotta-type Elbe sandstone (LG 16)	0.22	3.3	33.2	18.7	0.56	Siedel et al. (2010)

(continued on next page)

Table 6 (continued)

Sandstone	Porosity	Clay content (%)	Dry UCS (MPa)	Wet UCS (MPa)	UCS _{wet} / UCS _{dry}	Reference
Cotta-type Elbe sandstone (LG XVII)	0.21	4.7	39.7	17.7	0.45	Siedel et al. (2010)
Cotta-type Elbe sandstone (Neu 21)	0.22	4.8	21.1	18.9	0.90	Siedel et al. (2010)
Cotta-type Elbe sandstone (Neu 22)	0.23	3.1	19.8	15.8	0.80	Siedel et al. (2010)
Cotta-type Elbe sandstone (Neu Co)	0.192	4.8	45.0	26.5	0.59	Siedel et al. (2010)
Cotta-type Elbe sandstone (UK 12/1)	0.224	2.9	51.8	41.6	0.80	Siedel et al. (2010)
Cotta-type Elbe sandstone (UK 12/2)	0.223	3.4	39.2	28.6	0.73	Siedel et al. (2010)
Cotta-type Elbe sandstone (OK 13/1)	0.229	3.0	43.0	32.9	0.77	Siedel et al. (2010)
Cotta-type Elbe sandstone (Pow 15/1)	0.221	2.4	45.6	43.1	0.95	Siedel et al. (2010)
Cotta-type Elbe sandstone (Hor 16/1)	0.213	2.5	47.8	43.9	0.92	Siedel et al. (2010)
Cotta-type Elbe sandstone (RD A)	0.262	3.1	31.0	25.6	0.83	Siedel et al. (2010)
Cotta-type Elbe sandstone (RD B)	0.234	3.1	46.2	34.8	0.75	Siedel et al. (2010)
Cotta-type Elbe sandstone (RD C)	0.222	2.0	56.9	50.7	0.89	Siedel et al. (2010)
Posta-type Elbe sandstone (ML 1)	0.194	1.8	64.6	65.7	1.02	Siedel et al. (2010)
Posta-type Elbe sandstone (ML 2)	0.217	1.3	51.3	58.2	1.14	Siedel et al. (2010)
Posta-type Elbe sandstone (ML 3)	0.225	1.6	51.4	52.7	1.03	Siedel et al. (2010)
Posta-type Elbe sandstone (Her H)	0.21	0.0	57.6	45.6	0.79	Siedel et al. (2010)
Posta-type Elbe sandstone (Her II)	0.208	1.2	55.1	50.8	0.92	Siedel et al. (2010)
Posta-type Elbe sandstone (Her III)	0.222	1.5	53.2	45.2	0.85	Siedel et al. (2010)
Posta-type Elbe sandstone (Her IV)	0.193	1.1	54.8	43.6	0.80	Siedel et al. (2010)
Posta-type Elbe sandstone (Her V)	0.217	1.5	45.0	47.6	1.06	Siedel et al. (2010)
Posta-type Elbe sandstone (Zei 6/1)	0.22	0.8	58.2	49.2	0.85	Siedel et al. (2010)
Posta-type Elbe sandstone (Zei 6/2)	0.226	0.0	58.8	53.8	0.92	Siedel et al. (2010)
Posta-type Elbe sandstone (Zei 6/3)	0.228	0.9	53.1	45.5	0.86	Siedel et al. (2010)
Posta-type Elbe sandstone (Zei 6/4)	0.228	0.8	53.8	48.4	0.90	Siedel et al. (2010)
Posta-type Elbe sandstone (OV 7/1)	0.234	1.0	43.5	44.0	1.01	Siedel et al. (2010)
Posta-type Elbe sandstone (OV 7/2)	0.186	1.5	75.9	62.7	0.83	Siedel et al. (2010)
Posta-type Elbe sandstone (Mo 8/1)	0.204	0.6	46.1	42.2	0.92	Siedel et al. (2010)
Posta-type Elbe sandstone (Mo 8/2)	0.196	0.9	55.6	53.5	0.96	Siedel et al. (2010)
Posta-type Elbe sandstone (Sch 9/1)	0.242	0.8	37.1	37.9	1.02	Siedel et al. (2010)
Posta-type Elbe sandstone (Sch 9/2)	0.231	1.0	43.8	37.3	0.85	Siedel et al. (2010)
Posta-type Elbe sandstone (OK 13/2)	0.229	1.6	53.2	45.4	0.85	Siedel et al. (2010)
Posta-type Elbe sandstone (WB 14/1)	0.229	0.7	50.3	41.2	0.82	Siedel et al. (2010)
Posta-type Elbe sandstone (WB 14/2)	0.237	1.3	50.5	41.4	0.82	Siedel et al. (2010)
Posta-type Elbe sandstone (Pow 15/2)	0.251	1.2	36.9	22.4	0.61	Siedel et al. (2010)
Posta-type Elbe sandstone (Gri 17/1)	0.214	0.4	57.8	57.6	1.00	Siedel et al. (2010)
Grampians sandstone (10° angle)	0.09	6.2	59.7	50.4	0.84	Wasantha and Ranjith (2014)
Grampians sandstone (20° angle)	0.09	6.2	58.8	47.0	0.80	Wasantha and Ranjith (2014)
Grampians sandstone (35° angle)	0.09	6.2	53.7	46.5	0.87	Wasantha and Ranjith (2014)
Grampians sandstone (55° angle)	0.09	6.2	45.9	39.8	0.87	Wasantha and Ranjith (2014)
Grampians sandstone (83° angle)	0.09	6.2	57.4	49.7	0.87	Wasantha and Ranjith (2014)

This model, based on the classic work of Griffiths, has been previously used to describe the brittle failure of porous sandstones (e.g., Baud et al., 2014). The micromechanical model of Sammis and Ashby (1986) is an inclusion model comprising a two-dimensional elastic medium populated by circular holes of uniform radius, r . As the stress on the medium increases, cracks nucleate and propagate from the circular holes (parallel to the direction of the applied stress) when the stress intensity at the tip of a small crack on the circular surface reaches a critical value (K_{IC} , the fracture toughness). The cracks interact once they are long enough, thus increasing the local tensile stress intensity. Eventually, the cracks coalesce and conspire to induce the macroscopic failure of the elastic medium. In the case of uniaxial compression, Zhu et al. (2010) provide an analytical approximation of Sammis and Ashby's (1986) model to estimate UCS as a function of porosity, ϕ :

$$C_0 = \frac{1.325}{\phi^{0.414}} \frac{K_{IC}}{\sqrt{\pi r}} \quad (15)$$

Assuming that Eq. (15) can capture the behaviour of the sandstones of Table 6, there are three variables that influence uniaxial compressive strength: the porosity, ϕ , the fracture toughness, K_{IC} , and the pore radius, r . If we assume that the porosity and pore radius are the same for a given sandstone then, according to Eq. (15), the observed water-weakening (Fig. 12) must be due to a decrease in K_{IC} . Fig. 13 shows strength as a function of porosity using Eq. (15) for a fixed pore radius (125 μm) and different values of K_{IC} ($K_{IC} = 0.1, 0.3, 0.5$, and $0.8 \text{ MPa m}^{-1/2}$) alongside the dry (white circles) and wet (blue squares) data for the compiled sandstones. These modelled curves aptly demonstrate that decreasing the K_{IC} at a given porosity and pore size

lowers the strength (Fig. 13). The reduction in uniaxial compressive strength observed in wet rocks has been attributed to a reduction in fracture surface free energy due to the adsorption of water on the fracture surface (e.g., Parks, 1984; Baud et al., 2000). We conclude here, in line with the conclusions of Baud et al. (2000), that a lower fracture surface free energy in the presence of water reduces K_{IC} and therefore strength. Additionally, we highlight that water adsorption on clay minerals is extremely efficient due to their large surface areas. To emphasise, the specific surface areas of samples 157 (clay content = 2 wt.%) and 540 (clay content = 13.1 wt.%) are 204 and 6170 m²/kg, respectively (Heap et al., 2017; Tables 1 and 2). Therefore, a higher clay content should ensure that more water is adsorbed on the surface of the fracture, perhaps explaining the correlation between clay content and water-weakening (Fig. 12b). The scatter in the data of Fig. 12b suggests that clay content does not govern water-weakening in sandstones alone. One factor likely to play a key role is whether the clays are pore-coating or pore-filling, or whether the clays are present within the rock matrix. For water adsorption on clay minerals to influence the fracture surface free energy, the clays must be present within the material through which the fracture propagates (i.e. the matrix). By contrast, pore-coating clays may not exert a significant influence on the water-weakening process.

We further highlight that the micromechanics of low-porosity rocks is often described using the wing-crack model of Ashby and Sammis (1990), although we note that no or few microcracks were found in the intact microstructure of the studied materials (Fig. 3). If the wing-crack model was considered appropriate for the low-porosity materials studied herein, then there is an additional micromechanical

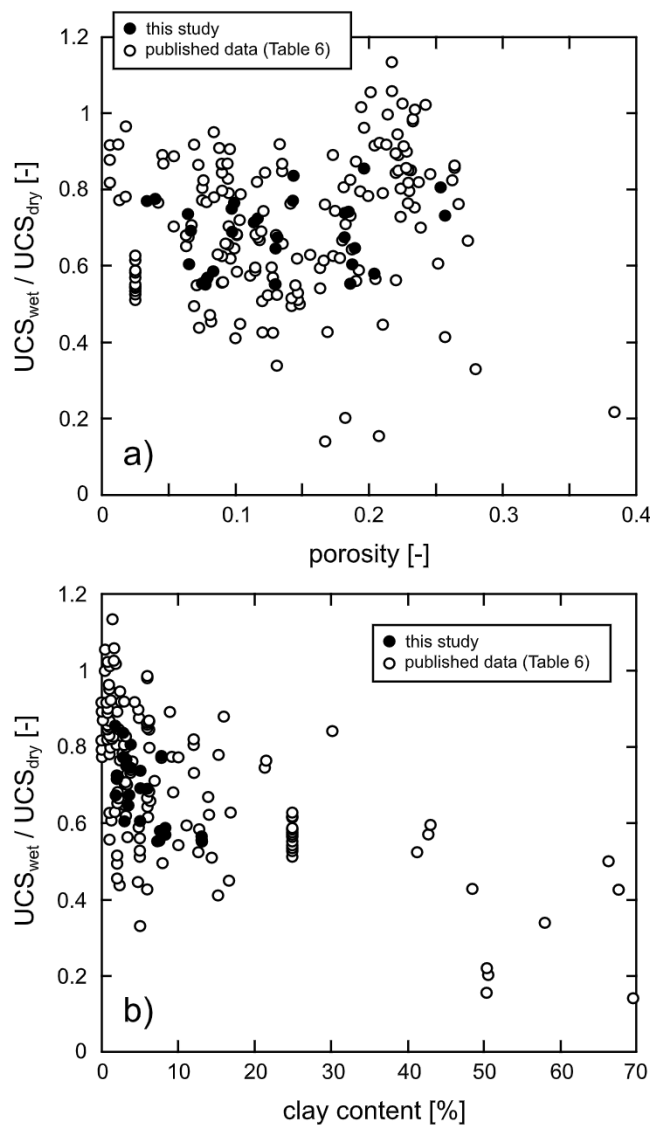


Fig. 12. (a) The ratio of wet to dry uniaxial compressive strength for the data unique to this study (Table 3) and data from published studies (Table 6) as a function of connected porosity. (b) The ratio of wet to dry uniaxial compressive strength for the data unique to this study (Table 3) and data from published studies (Table 6) as a function of clay content.

parameter—the coefficient of friction—could also be influenced by the presence of water.

5.2. Implications for geothermal energy exploitation

We have provided estimates of the rock mass strength (Fig. 11b) and elastic modulus (Fig. 11c) for the Buntsandstein sedimentary sequence (from the Soultz-sous-Forêts geothermal site) that directly overlies the fractured granitic basement used throughout the Upper Rhine Graben as a geothermal resource. One of the main motivations for this study is that recent (e.g., Rittershoffen; Baujard et al., 2017) and future geothermal exploitation in the Upper Rhine Graben has and will target rock at or close to this interface. Since the Buntsandstein is known to be a laterally extensive unit (e.g. Aichholzer et al., 2016; Vidal and Genter, 2018), these new reservoir-scale strength and elastic modulus estimates could assist prospection, stimulation, and optimisation strategies (for instance, the Buntsandstein was stimulated at the Rittershoffen site in 2013; Vidal et al., 2016; Baujard et al., 2017) at geothermal sites within the Upper Rhine Graben. We can combine our strength and elastic

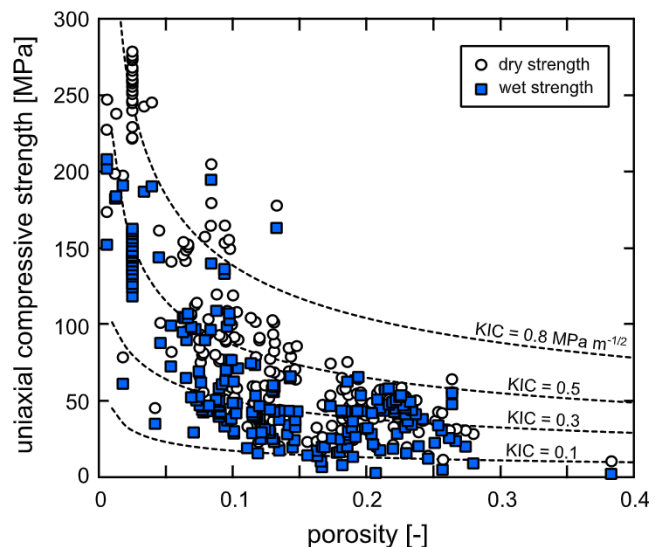


Fig. 13. Dry (white circles) and wet (blue squares) uniaxial compressive strength data (data unique to this study (Table 3) and published data (Table 6)) as a function of porosity. Modelled curves, using Eq. (15), show curves of uniaxial compressive strength as a function of porosity for a fixed pore radius (125 μm) and different values of K_{IC} ($K_{IC} = 0.1, 0.3, 0.5$, and $0.8 \text{ MPa m}^{-1/2}$) (see text for details). (For interpretation of the references to colour in this figure legend, the reader is referred to the web version of this article).

modulus estimates for the Buntsandstein with those for the granite reservoir provided in Villeneuve et al. (2018) to give strength (Fig. 14b) and elastic modulus (Fig. 15b) estimates for the EPS-1 borehole from a depth of ~1000 to ~2200 m. These data highlight, for example, that the rock mass strength of the granitic reservoir can be lower than that for the Buntsandstein, due to the high fracture density of the granite (Fig. 14).

However, since the rock mass strength and elastic modulus estimations (Fig. 11b, c, 14b, and 15b) are very much dependent on the fracture density (and their surface condition), the estimations provided herein may not be directly applicable to the Buntsandstein sedimentary sequence found at other geothermal sites, which will likely be characterised by different fracture densities and intersect regional scale faults at different depths. For example, the Buntsandstein is much deeper at the Rittershoffen site (from ~1800 to ~2200 m; Aichholzer et al., 2016) than at Soultz-sous-Forêts and major fracture zones are found at depths of ~1975, ~1986, and ~2140 m (Vidal et al., 2017). Further, the extent of fracture infilling will also be spatially variable. For instance, Vidal et al. (2015) note that the extent of the fracture sealing can differ in the same fractured zone at different wells (e.g., GPK-2, GPK-3, and GPK-4, which are separated by no more than 1.5 km) at Soultz-sous-Forêts. We further note that the sedimentary units overlying the granitic reservoir can be appreciably different from those at the Soultz-sous-Forêts site at a distance of several tens of kilometres (Kushnir et al., 2018b). However, we highlight that our laboratory data can be re-used to provide upscaled strength and elastic modulus profiles for other sites, using the methods outlined herein, as long as site-specific rock mass descriptions are performed. We highlight that direct core data will provide a more complete characterisation of the fracture network than borehole imaging tools (Genter et al., 1997). A recent study by Bauer et al. (2017) also highlights that, when core materials are not available, care should be taken when selecting outcrop analogues for geothermal reservoir rock.

Our laboratory data have shown that the Buntsandstein sandstones are weaker when wet (Fig. 5). In zones characterised by the intact rock strength and elastic modulus (i.e. all zones except the five highly fractured zones) (Fig. 11b and c), the reservoir-scale strength and the elastic modulus are lower when the rock is wet. Differences between the

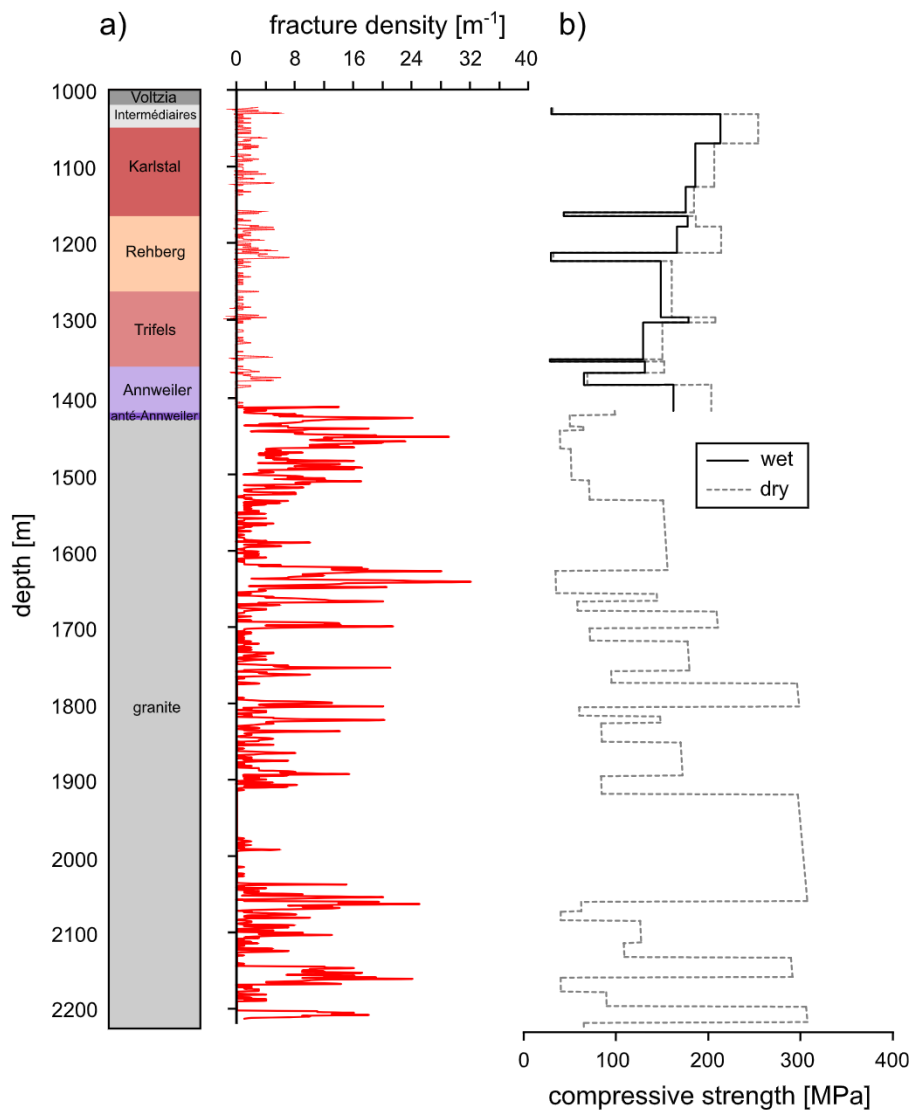


Fig. 14. (a) Stratigraphic column of exploration well EPS-1 at Soultz-sous-Forêts (from 1012 to 2200 m) next to the fracture density data for the core. (b) Wet (black line) and dry (grey dashed line) rock mass compressive strength. Note that dry and wet values are given for the Buntsandstein (interval 1012–1416 m) only.

dry and wet strength and elastic modulus within the five fractured zones are small: the strength and elastic modulus in these zones is primarily dictated by the rock mass structure (fractures) (Fig. 11b and c). Since the pore space of rocks within a geothermal reservoir will be saturated with liquid water/brine in-situ, our measurements and analysis therefore highlight the importance of performing wet deformation experiments to provide upscaled strength and elastic modulus assessments for geothermal applications. Indeed, not only are the wet and dry strengths and elastic moduli different (Fig. 5), but we also measured a difference between the dry and wet m_i term (Fig. 9). We recommend that future studies that adopt this technique also perform wet deformation experiments, particularly because water-weakening has been reported in a wide range of rock types (e.g., sandstone: Hawkins and McConnell, 1992, tuff: Zhu et al., 2011; Heap et al., 2018, basalt: Zhu et al., 2016, carbonates: Baud et al., 2016).

Although we performed wet deformation measurements to provide more accurate strength and elastic modulus assessments, we highlight that our experiments were performed at room temperature and used deionised water. First, the temperature of the Buntsandstein rocks at Soultz-sous-Forêts, for example, is between 120 and 140 °C (e.g., Genter et al., 2010). The intact strength and stiffness of sandstone measured in the laboratory may be different at high-temperature, although there is a

paucity of data. For example, Ranjith et al. (2012) found that the uniaxial compressive strength and stiffness of Hawkesbury sandstone (containing 20% clay) increased from 36.5 to 42.5 MPa and from 2.8 to 3.3 GPa, respectively, as the testing temperature was increased from 25 to 200 °C. Rao et al. (2007) also observed an increase in uniaxial compressive strength and stiffness for sandstone as temperature was increased from 25 to 150 °C. Therefore, based on these few data, it would appear that the rock mass strength and elastic modulus assessments provided herein (measured at room temperature) may underestimate the strength and elastic modulus of the rock in-situ. However, firm conclusions cannot be drawn without further experimental investigations. For example, Heap et al. (2009a) showed that the compressive strength of three sandstones under triaxial testing conditions (an effective pressure of 30 MPa) was slightly lower at 75 °C than at room temperature. At present it is unclear as to the influence of, for example, mineral content, porosity, and grain size on the compressive strength of sandstone at high-temperature. Second, the rocks within the reservoir are saturated with hydrothermal brines with a pH between 5.2 and 5.5 (e.g., Scheiber et al., 2012). A lower pH should reduce the fracture surface free energy (e.g., Parks, 1984) and therefore reduce intact strength. Indeed, Singh et al. (1999) measured a reduction in uniaxial compressive strength in sandstone from ~65 to ~40 MPa as

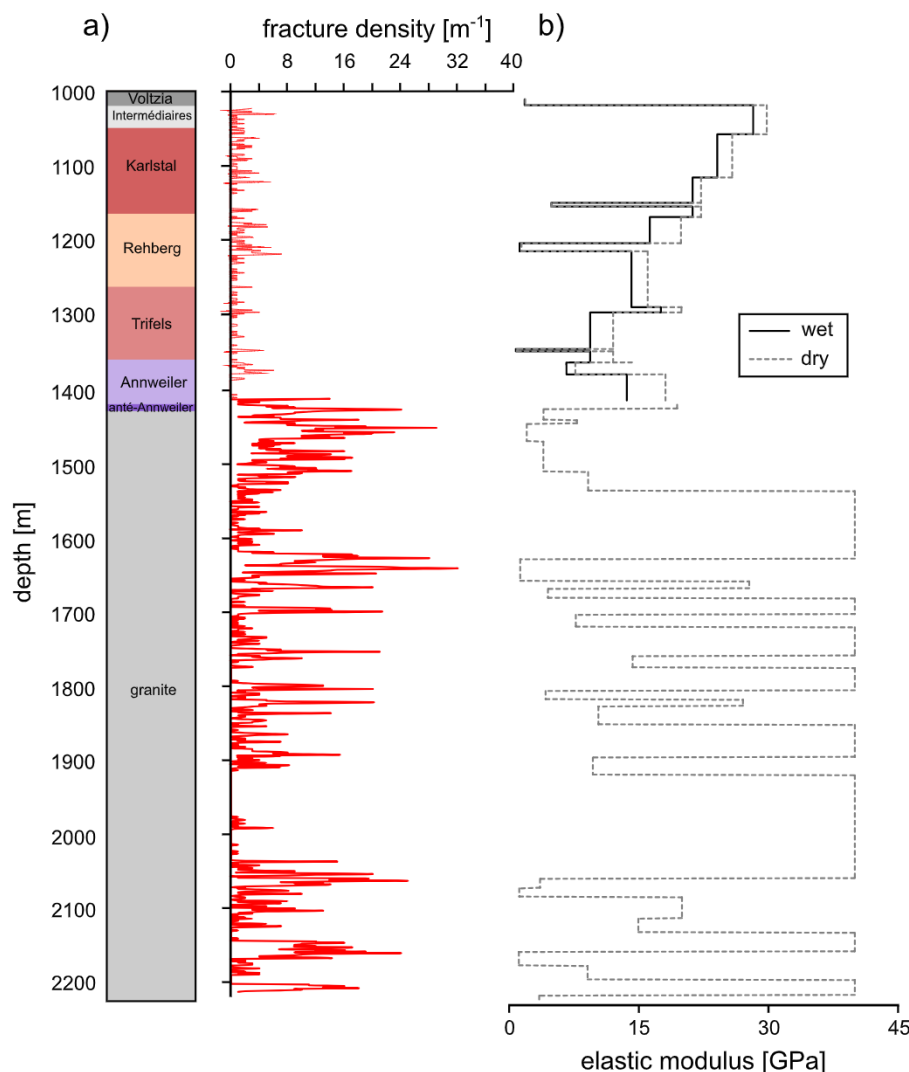


Fig. 15. (a) Stratigraphic column of exploration well EPS-1 at Soultz-sous-Forêts (from 1012 to 2200 m) next to the fracture density data for the core. (b) Wet (black line) and dry (grey dashed line) rock mass elastic modulus. Note that dry and wet values are given for the Buntsandstein (interval 1012–1416 m) only.

the pH was reduced from 7 to 2. The uniaxial compressive strength of sandstone samples was also found to first decrease and then increase with increasing salinity (Shukla et al., 2013; Rathnaweera et al., 2014). However, recent triaxial experiments showed that the triaxial compressive strength of sandstone increased with increasing NaCl concentration (Huang et al., 2018). It is therefore difficult to draw firm conclusions as to the influence of the pore fluid composition and pH on the strength and stiffness of sandstone without further laboratory testing.

We highlight that the reservoir-scale strength and elastic modulus estimates provided here are representative of the short-term strength. These rock properties, and empirical term m_i , were all determined at a laboratory strain rate of $1 \times 10^{-6} \text{ s}^{-1}$. Although this strain rate is an order of magnitude lower than typically used in laboratory testing, we highlight that the strength of rock, including sandstone, decreases as strain rate is decreased due to time-dependent subcritical crack growth processes (Atkinson, 1984; Brantut et al., 2013). There have been many experimental studies on time-dependent deformation in sandstone (e.g., Ngwenya et al., 2001; Baud and Meredith, 1997; Heap et al., 2009a, 2009b; Yang and Jiang, 2010; Brantut et al., 2014; Tang et al., 2018). For example, Heap et al. (2009b) showed that sandstone fails at 80% of its short-term failure stress in about 60 h. Further, and pertinent to the geothermal reservoir case study, the deformation rate during a brittle creep test can increase by up to three orders of magnitude as the

temperature is increased from 20 to 75 °C (Heap et al., 2009a). Based on the data provided in these studies, the long-term strength of the Buntsandstein sedimentary sequence may be lower than the short-term strength estimates provided herein.

6. Concluding remarks

Recent geothermal exploitation in the Upper Rhine Graben has targeted the interface between the fractured granitic basement and the overlying Permian and Triassic sedimentary rocks (the Buntsandstein), and geothermal projects being developed in the region will continue to do so. Our study provides wet and dry strength and elastic modulus estimates for the Buntsandstein sedimentary sequence (from 1008 to 1414 m) at the Soultz-sous-Forêts geothermal site in France. To provide such estimates we performed 64 uniaxial (32 dry and 32 wet) and 10 triaxial deformation experiments (5 dry and 5 wet). These data were coupled with Geological Strength Index (GSI) assessments to provide down-well wet and dry strength and elastic modulus profiles using the Hoek-Brown failure criterion and the Hoek-Diederichs equation, respectively. Our analysis finds five zones characterised by low values of GSI (zones with high fracture densities and infilling thicknesses) that have low values of rock mass strength and elastic modulus. The zones with low fracture densities (i.e. a “massive” rock structure) are characterised by the intact rock properties (i.e. a GSI value of 100) and

therefore have higher values of strength and elastic modulus. Additionally, we find that the strength and elastic modulus of these massive zones are lower when the rock is wet, highlighting the importance of performing wet deformation experiments for rock mass assessments of rock that is typically saturated with a liquid phase, such as in a geothermal reservoir. We combine these new data with those for the underlying fractured granite reservoir to produce down-well strength and elastic modulus profiles from a depth of ~1000 to ~2200 m for the Soultz-sous-Forêts geothermal site. Although this type of analysis is somewhat site specific, the methods used and data provided herein can be easily adapted to provide strength and elastic modulus estimates for other geothermal sites within the Upper Rhine Graben to assist reservoir prospection, stimulation, and optimisation strategies.

Author contributions

M.J. Heap led the project and co-wrote the manuscript with M. Villeneuve. P. Baud, M.J. Heap, and A.R.L. Kushnir chose and collected the samples from the Merkwiller core repository. M.J. Heap and A.R.L. Kushnir measured the porosity of the experimental samples. M.J. Heap performed all the uniaxial compressive strength tests. M.J. Heap, A.R.L. Kushnir, and J.I. Farquharson performed the triaxial compressive strength tests. M. Villeneuve performed the geotechnical analyses. All authors had a hand in the preparation of the manuscript and the interpretation of the data.

Acknowledgements

This study was funded by LABEX grant ANR-11-LABX-0050_G-EAU-THERMIE-PROFONDE (this research therefore benefited from state funding managed by the Agence National de la Recherche (ANR) as part of the “Investissements d’avenir” program) and ANR grant CANTARE (ANR-15-CE06-0014-01). We are extremely grateful to Albert Genter, who provided the fracture data from EPS-1 (we therefore also acknowledge the Bureau de Recherches Géologiques et Minières (BRGM)). We also wish to thank Chrystal Dezayes, Bertrand Renaudié, Coralie Aichholzer, and Philippe Düringer. The comments of two anonymous reviewers helped clarify certain aspects of this manuscript.

References

- Aichholzer, C., Düringer, P., Orciani, S., Genter, A., 2016. New stratigraphic interpretation of the Soultz-sous-Forêts 30-year-old geothermal wells calibrated on the recent one from Rittershoffen (Upper Rhine Graben, France). *Geotherm Energy* 4, 13.
- Ashby, M.F., Sammis, C.G., 1990. The damage mechanics of brittle solids in compression. *Pure Appl. Geophys.* 133, 489–521.
- Atkinson, B.K., 1984. Subcritical crack growth in geological materials. *J. Geophys. Res.: Solid Earth* 89, 4077–4114.
- Baillieux, P., Schill, E., Edel, J.B., Mauri, G., 2013. Localization of temperature anomalies in the Upper Rhine Graben: insights from geophysics and neotectonic activity. *Int. Geol. Rev.* 55, 1744–1762.
- Baria, R., Baumgärtner, J., Gérard, A., Jung, R., Garnish, J., 1999. European HDR research programme at Soultz-sous-Forêts (France) 1987–1996. *Geothermics* 28 (4), 655–669.
- Baud, P., Meredith, P.G., 1997. Damage accumulation during triaxial creep of Darley Dale sandstone from pore volumetry and acoustic emission. *Int. J. Rock Mech. Min. Sci.* 34, 24-e1.
- Baud, P., Zhu, W., Tf, Wong, 2000. Failure mode and weakening effect of water on sandstone. *J. Geophys. Res.: Solid Earth* 105 (B7), 16371–16389.
- Baud, P., Louis, L., David, C., Rawling, G.C., Tf, Wong, 2005. Effects of Bedding and Foliation on Mechanical Anisotropy, Damage Evolution and Failure Mode 245. Geological Society, London, Special Publications, pp. 223–249.
- Baud, P., Tf, Wong, Zhu, W., 2014. Effects of porosity and crack density on the compressive strength of rocks. *Int. J. Rock Mech. Min. Sci.* 67, 202–211.
- Baud, P., Reuschlé, T., Ji, Y., Cheung, C.S., Tf, Wong, 2015. Mechanical compaction and strain localization in Bleurswiller sandstone. *J. Geophys. Res.: Solid Earth* 120 (9), 6501–6522.
- Baud, P., Rolland, A., Heap, M.J., Xu, T., Nicolé, M., Ferrand, T., Reuschlé, T., Toussaint, R., Conil, N., 2016. Impact of stylolites on the mechanical strength of limestone. *Tectonophysics* 690, 4–20.
- Bauer, J.F., Krumbholz, M., Meier, S., Tanner, D.C., 2017. Predictability of properties of a fractured geothermal reservoir: the opportunities and limitations of an outcrop analogue study. *Geothermal Energy* 5 (1), 24.
- Baujard, C., Genter, A., Dalmais, E., Maurer, V., Hehn, R., Rosillette, R., Vidal, J., Schmittbuhl, J., 2017. Hydrothermal characterization of wells GRT-1 and GRT-2 in Rittershoffen, France: implications on the understanding of natural flow systems in the Rhine graben. *Geothermics* 65, 255–268.
- Bell, F.G., 1995. Laboratory testing of rocks. In: Bell, F.G. (Ed.), *Engineering in Rock*, pp. 151–169.
- Bell, F.G., 1978. Petrographical factors relating to porosity and permeability in the Fell Sandstone. *Q. J. Eng. Geol. Hydrogeol.* 11 (2), 113–126.
- Bell, F.G., Culshaw, M.G., 1998. Petrographic and engineering properties of sandstones from the Sneinton Formation, Nottinghamshire, England. *Q. J. Eng. Geol. Hydrogeol.* 31 (1), 5–19.
- Bésuelle, P., Baud, P., Wong, Tf, 2003. Failure mode and spatial distribution of damage in Rothbach sandstone in the brittle-ductile transition. *Pure Appl. Geophys.* 160 (5–6), 851–868.
- Brace, W.F., Paulding Jr, B.W., Scholz, C.H., 1966. Dilatancy in the fracture of crystalline rocks. *J. Geophys. Res.* 71, 3939–3953.
- Brantut, N., Heap, M.J., Meredith, P.G., Baud, P., 2013. Time-dependent cracking and brittle creep in crustal rocks: a review. *J. Struct. Geol.* 52, 17–43.
- Brantut, N., Heap, M.J., Baud, P., Meredith, P.G., 2014. Rate-and strain-dependent brittle deformation of rocks. *J. Geophys. Res.: Solid Earth* 119, 1818–1836.
- Buchmann, T.J., Connolly, P.T., 2007. Contemporary kinematics of the Upper Rhine Graben: a 3D finite element approach. *Glob. Planet. Change* 58, 287–309.
- Chang, C., Zoback, M.D., Khaksar, A., 2006. Empirical relations between rock strength and physical properties in sedimentary rocks. *J. Petrol. Sci. Eng.* 51, 223–237.
- Cuss, R.J., Rutter, E.H., Holloway, R.F., 2003. The application of critical state soil mechanics to the mechanical behaviour of porous sandstones. *Int. J. Rock Mech. Min. Sci.* 40 (6), 847–862.
- David, C., Wong, T.F., Zhu, W., Zhang, J., 1994. Laboratory measurement of compaction-induced permeability change in porous rocks: implications for the generation and maintenance of pore pressure excess in the crust. *Pure Appl. Geophys.* 143 (1–3), 425–456.
- Demarco, M.M., Jahns, E., Rüdrich, J., Oyhancabal, P., Siegesmund, S., 2007. The impact of partial water saturation on rock strength: an experimental study on sandstone [Der Einfluss einer partiellen Wassersättigung auf die mechanischen Gesteins-eigenschaften: eine Fallstudie an Sandsteinen]. *Zeitschrift der Deutschen Gesellschaft für Geowissenschaften* 58 (4), 869–882.
- Dezayes, C., Genter, A., Valley, B., 2010. Structure of the low permeable naturally fractured geothermal reservoir at Soultz. *C.R. Geosci.* 342, 517–530.
- Dyke, C.G., Dobereiner, L., 1991. Evaluating the strength and deformability of sandstones. *Q. J. Eng. Geol. Hydrogeol.* 24, 123–134.
- Eberhardt, E., 2012. The Hoek-Brown failure criterion. In: Ulusay, R. (Ed.), *The ISRM Suggested Methods for Rock Characterization, Testing and Monitoring: 2007–2014*, pp. 233–240.
- Freymark, J., Sippel, J., Scheck-Wenderoth, M., Bär, K., Stiller, M., Fritsche, J.G., Kracht, M., 2017. The deep thermal field of the Upper Rhine Graben. *Tectonophysics* 694, 114–129.
- Genter, A., Traineau, H., 1996. Analysis of macroscopic fractures in granite in the HDR geothermal well EPS-1, Soultz-sous-Forêts, France. *J. Volcanol. Geotherm. Res.* 72, 121–141.
- Genter, A., Castaing, C., Dezayes, C., Tenzer, H., Traineau, H., Villemain, T., 1997. Comparative analysis of direct (core) and indirect (borehole imaging tools) collection of fracture data in the Hot Dry Rock Soultz reservoir (France). *J. Geophys. Res.: Solid Earth* 102, 15419–15431.
- Genter, A., Evans, K., Cuenot, N., Fritsch, D., Sanjuan, B., 2010. Contribution of the exploration of deep crystalline fractured reservoir of Soultz to the knowledge of enhanced geothermal systems (EGS). *C.R. Geosci.* 342, 502–516.
- Gérard, A., Genter, A., Kohl, T., 2006. The deep EGS (enhanced geothermal system) project at Soultz-sous-Forêts (Alsace, France). *Geothermics* 35, 473–483.
- Glaas, C., Genter, A., Girard, J.F., Patrier, P., Vidal, J., 2018. How do the geological and geophysical signatures of permeable fractures in granitic basement evolve after long periods of natural circulation? Insights from the Rittershoffen geothermal wells (France). *Geotherm Energy* 6, 14.
- Griffiths, L., Heap, M.J., Wang, F., Daval, D., Gilg, H.A., Baud, P., Schmittbuhl, J., Genter, A., 2016. Geothermal implications for fracture-filling hydrothermal precipitation. *Geothermics* 64, 235–245.
- Guillou-Frottier, L., Carré, C., Bourgine, B., Bouchot, V., Genter, A., 2013. Structure of hydrothermal convection in the Upper Rhine Graben as inferred from corrected temperature data and basin-scale numerical models. *J. Volcanol. Geotherm. Res.* 256, 29–49.
- Hadizadeh, J., Law, R.D., 1991. Water-weakening of sandstone and quartzite deformed at various stress and strain rates. *Int. J. Rock Mech. Min. Sci. Geomech. Abs.* 28, 431–439.
- Haffen, S., Géraud, Y., Diraison, M., Dezayes, C., 2013. Determination of fluid-flow zones in a geothermal sandstone reservoir using thermal conductivity and temperature logs. *Geothermics* 46, 32–41.
- Hawkins, A.B., McConnell, B.J., 1992. Sensitivity of sandstone strength and deformability to changes in moisture content. *Q. J. Eng. Geol. Hydrogeol.* 25, 115–130.
- Heap, M.J., Baud, P., Meredith, P.G., 2009a. Influence of temperature on brittle creep in sandstones. *Geophys. Res. Lett.* 36 (19). <https://doi.org/10.1029/2009GL039373>.
- Heap, M.J., Baud, P., Meredith, P.G., Bell, A.F., Main, I.G., 2009b. Time-dependent brittle creep in Darley Dale sandstone. *J. Geophys. Res.: Solid Earth* 114 (B7). <https://doi.org/10.1029/2008JB006212>.
- Heap, M.J., Lavallée, Y., Petrakova, L., Baud, P., Reuschlé, T., Varley, N.R., Dingwell, D.B., 2014. Microstructural controls on the physical and mechanical properties of edifice-forming andesites at Volcán de Colima, Mexico. *J. Geophys. Res.: Solid Earth*

- 119 (4), 2925–2963.
- Heap, M.J., Kushnir, A.R.L., Gilg, H.A., Wadsworth, F.B., Reuschlé, T., Baud, P., 2017. Microstructural and petrophysical properties of the Permo-Triassic sandstones (Buntsandstein) from the Soultz-sous-Forêts geothermal site (France). *Geotherm. Energy* 5 (1), 26.
- Heap, M.J., Farquharson, J.I., Kushnir, A.R., Lavallée, Y., Baud, P., Gilg, H.A., Reuschlé, T., 2018. The influence of water on the strength of Neapolitan Yellow Tuff, the most widely used building stone in Naples (Italy). *Bull. Volcanol.* 80 (6), 51.
- Hoek, E., 2007. Practical Rock Engineering. E-Book. <https://www.rocscience.com/learning/hoek-s-corner/books>.
- Hoek, E., Bieniawski, Z.T., 1965. Brittle fracture propagation in rock under compression. *Int. J. Fract.Mech.* 1, 137–155.
- Hoek, E., Brown, E.T., 1980. Empirical strength criterion for rock masses. *J. Geotech. Geoenviron. Eng.* 106 (GT9), 1013–1035.
- Hoek, E., Brown, E.T., 1997. Practical estimates of rock mass strength. *Int. J. Rock Mech. Min. Sci.* 34 (8), 1165–1186.
- Hoek, E., Diederichs, M.S., 2006. Empirical estimation of rock mass modulus. *Int. J. Rock Mech. Min. Sci.* 43 (2), 203–215.
- Hoek, E., Carranza-Torres, C.T., Corkum, B., 2002. Hoek–Brown failure criterion—2002 edition. In: Hammah, R., Bawden, W., Curran, J., Telesnicki, M. (Eds.), Proceedings of the Fifth North American Rock Mechanics Symposium (NARMS-TAC). University of Toronto Press, Toronto, pp. 267–273.
- Huang, Y.H., Yang, S.Q., Hall, M.R., Zhang, Y.C., 2018. The effects of NaCl concentration and confining pressure on mechanical and acoustic behaviors of brine-saturated sandstone. *Energies* 11 (2), 385.
- Kappelmeyer, O., Gérard, A., Schloemer, W., Ferrandes, R., Rummel, F., Benderitter, Y., 1991. European HDR project at Soultz-sous-Forêts: general presentation. *Geotherm. Sci. Technol.* 2 (4), 263–289.
- Kasim, M., Shakoor, A., 1996. An investigation of the relationship between uniaxial compressive strength and degradation for selected rock types. *Eng. Geol.* 44 (1–4), 213–227.
- Kushnir, A.R.L., Heap, M.J., Baud, P., 2018a. Assessing the role of fractures on the permeability of the Permo-Triassic sandstones at the Soultz-sous-Forêts (France) geothermal site. *Geothermics* 74, 181–189.
- Kushnir, A.R., Heap, M.J., Baud, P., Gilg, H.A., Reuschlé, T., Lerouge, C., Dezayes, C., Duringer, P., 2018b. Characterizing the physical properties of rocks from the Paleozoic to Permo-Triassic transition in the Upper Rhine Graben. *Geotherm. Energy* 6, 16.
- Lin, M.L., Jeng, F.S., Tsai, L.S., Huang, T.H., 2005. Wetting weakening of tertiary sandstones—microscopic mechanism. *Environ. Geol.* 48 (2), 265–275.
- Louis, L., David, C., Metz, V., Robion, P., Menendez, B., Kissel, C., 2005. Microstructural control on the anisotropy of elastic and transport properties in undeformed sandstones. *Int. J. Rock Mech. Min. Sci.* 42 (7–8), 911–923.
- Louis, L., Baud, P., Wong, T.F., 2009. Microstructural inhomogeneity and mechanical anisotropy associated with bedding in Rothbach sandstone. *Pure Appl. Geophys.* 166 (5–7), 1063–1087.
- Magnenet, V., Fond, C., Genter, A., Schmittbuhl, J., 2014. Two-dimensional THM modelling of the large scale natural hydrothermal circulation at Soultz-sous-Forêts. *Geotherm. Energy* 2 (1), 17.
- Marinos, V., Marinos, P., Hoek, E., 2005. The geological strength index: applications and limitations. *Bull. Eng. Geol. Environ.* 64, 55–65.
- Nespereira, J., Blanco, J.A., Yenes, M., Pereira, D., 2010. Irregular silica cementation in sandstones and its implication on the usability as building stone. *Eng. Geol.* 115 (3–4), 167–174.
- Ngwenya, B.T., Main, I.G., Elphick, S.C., Crawford, B.R., Smart, B.G., 2001. A constitutive law for low-temperature creep of water-saturated sandstones. *J. Geophys. Res.: Solid Earth* 106, 21811–21826.
- Palchik, V., 1999. Influence of porosity and elastic modulus on uniaxial compressive strength in soft brittle porous sandstones. *Rock Mech. Rock Eng.* 32, 303–309.
- Parks, G.A., 1984. Surface and interfacial free energies of quartz. *J. Geophys. Res.: Solid Earth* 89 (B6), 3997–4008.
- Paterson, M.S., Wong, Tf, 2005. Experimental Rock Deformation—the Brittle Field. Springer Science & Business Media.
- Pribnow, D., Schellschmidt, R., 2000. Thermal tracking of upper crustal fluid flow in the Rhine Graben. *Geophys. Res. Lett.* 27 (13), 1957–1960.
- Ranjith, P.G., Viete, D.R., Chen, B.J., Perera, M.S.A., 2012. Transformation plasticity and the effect of temperature on the mechanical behaviour of Hawkesbury sandstone at atmospheric pressure. *Eng. Geol.* 151, 120–127.
- Rao, Q.H., Wang, Z., Xie, H.F., Xie, Q., 2007. Experimental study of mechanical properties of sandstone at high temperature. *J. Central South Univ. Technol.* 14 (1), 478–483.
- Rathnaweera, T.D., Ranjith, P.G., Perera, M.S.A., 2014. Salinity-dependent strength and stress-strain characteristics of reservoir rocks in deep saline aquifers: an experimental study. *Fuel* 122, 1–11.
- Rocscience Inc. (2017) <https://www.rocscience.com>.
- Rutter, E.H., Mainprice, D.H., 1978. The effect of water on stress relaxation of faulted and unfaulted sandstone. *Rock Friction and Earthquake Prediction*. Birkhäuser, Basel, pp. 634–650.
- Sammis, C.G., Ashby, M.F., 1986. The failure of brittle porous solids under compressive stress states. *Acta Metall.* 34 (3), 511–526.
- Sausse, J., Fourar, M., Genter, A., 2006. Permeability and alteration within the Soultz granite inferred from geophysical and flow log analysis. *Geothermics* 35 (5–6), 544–560.
- Scheiber, J., Nitschke, F., Seibt, A., Genter, A., 2012. Geochemical and mineralogical monitoring of the geothermal power plant in Soultz-sous-Forêts (France). *Proceedings of the 37th Workshop on Geothermal Reservoir Engineering*, pp. 1033–1042.
- Scholz, C.H., 1968. Microfracturing and the inelastic deformation of rock in compression. *J. Geophys. Res.* 73, 1417–1432.
- Schultz, R.A., 1996. Relative scale and the strength and deformability of rock masses. *J. Struct. Geol.* 18 (9), 1139–1149.
- Shakoor, A., Barefield, E.H., 2009. Relationship between unconfined compressive strength and degree of saturation for selected sandstones. *Environ. Eng. Geosci.* 15 (1), 29–40.
- Shukla, R., Ranjith, P.G., Choi, S.K., Haque, A., Yellishetty, M., Hong, L., 2013. Mechanical behaviour of reservoir rock under brine saturation. *Rock Mech. Rock Eng.* 46, 83–93.
- Siedel, H., Pfefferkorn, S., von Plehwe-Leisen, E., Leisen, H., 2010. Sandstone weathering in tropical climate: results of low-destructive investigations at the temple of Angkor Wat, Cambodia. *Eng. Geol.* 115 (3–4), 182–192.
- Singh, T.N., Singh, S.K., Mishra, A., Singh, P.K., Singh, V.K., 1999. Effect of acidic water on physico-mechanical behaviour of rock. *Indian J. Eng. Mater. Sci.* 6, 66–72.
- Tang, S.B., Yu CY, Heap M.J., Chen, P.Z., Ren, Y.G., 2018. The influence of Water saturation on the short-and long-term mechanical behavior of red sandstone. *Rock Mech. Rock Eng.* 1–19.
- Ulusay, R., Hudson, J., 2007. The complete ISRM suggested methods for Rock characterization. Testing and Monitoring: 1974–2006. Elsevier, Antalya, Turkey.
- Vásárhelyi, B., Ván, P., 2006. Influence of water content on the strength of rock. *Eng. Geol.* 84 (1–2), 70–74.
- Vernoux, J.F., Genter, A., Razin, P., Vinchon, C., 1995. Geological and petrophysical parameters of a deep fractured sandstone formation as applied to geothermal exploitation. *BRGM Report 38622*. pp. 70.
- Vidal, J., Genter, A., 2018. Overview of naturally permeable fractured reservoirs in the central and southern Upper Rhine Graben: insights from geothermal wells. *Geothermics* 74, 57–73.
- Vidal, J., Genter, A., Schmittbuhl, J., 2015. How do permeable fractures in the Triassic sediments of Northern Alsace characterize the top of hydrothermal convective cells? Evidence from Soultz geothermal boreholes (France). *Geotherm. Energy* 3, 8.
- Vidal, J., Genter, A., Schmittbuhl, J., 2016. Pre-and post-stimulation characterization of geothermal well GRT-1, Rittershoffen, France: insights from acoustic image logs of hard fractured rock. *Geophys. J. Int.* 206, 845–860.
- Vidal, J., Genter, A., Chopin, F., 2017. Permeable fracture zones in the hard rocks of the geothermal reservoir at Rittershoffen, France. *J. Geophys. Res.: Solid Earth* 122, 4864–4887.
- Villeneuve, M., Heap, M.J., Kushnir, A.R.L., Qin, T., Baud, P., Zhou, G., Xu, T., 2018. Estimating in-situ rock mass strength and elastic modulus of granite from the Soultz-sous-Forêts geothermal reservoir (France). *Geotherm. Energy* 6, 11.
- Wasantha, P.L., Ranjith, P.G., 2014. Water-weakening behavior of Hawkesbury sandstone in brittle regime. *Eng. Geol.* 178, 91–101.
- Wong, Tf, David, C., Zhu, W., 1997. The transition from brittle faulting to cataclastic flow in porous sandstones: mechanical deformation. *J. Geophys. Res.: Solid Earth* 102 (B2), 3009–3025.
- Yang, S.Q., Jiang, Y., 2010. Triaxial mechanical creep behavior of sandstone. *Mining Sci. Technol. (China)* 20 (3), 339–349.
- Zang, A., Wagner, C.F., Dresen, G., 1996. Acoustic emission, microstructure, and damage model of dry and wet sandstone stressed to failure. *J. Geophys. Res.: Solid Earth* 101 (B8), 17507–17521.
- Zhu, W., Baud, P., Tf, Wong, 2010. Micromechanics of cataclastic pore collapse in limestone. *J. Geophys. Res.: Solid Earth* 115 (B4). <https://doi.org/10.1029/2009JB006610>.
- Zhu, W., Baud, P., Vinciguerra, S., Tf, Wong, 2011. Micromechanics of brittle faulting and cataclastic flow in Alban Hills tuff. *J. Geophys. Res.: Solid Earth* 116 (B6).
- Zhu, W., Baud, P., Vinciguerra, S., Wong, Tf, 2016. Micromechanics of brittle faulting and cataclastic flow in Mount Etna basalt. *J. Geophys. Res.: Solid Earth* 121 (6), 4268–4289.